POLYIMIDE AEROGELS AND THEIR APPLICATIONS IN REMOVAL OF AIRBORNE NANOPARTICLES

A Thesis

Presented to

The Graduate Faculty of The University of Akron

In Partial Fulfillment

Of the Requirements for the Degree

Master of Science

Chunhao Zhai

Aug, 2016

POLYIMIDE AEROGELS AND THEIR APPLICATIONS IN REMOVAL OF AIRBORNE NANOPARTICLES

Chunhao Zhai

Thesis

Approved:	Accepted:
Advisor Dr. Sadhan C. Jana	Dean of the College Dr. Eric J. Amis
Faculty Reader Dr. Kevin A. Cavicchi	Dean of the Graduate School Dr. Chand Midha
Faculty Reader Dr. Younjin Min	Date
Department Chair Dr. Sadhan C. Jana	

ABSTRACT

Airborne particles are considered extremely hazardous to human health. The hazard level of these particles have an inverse relationship with the size. PM2.5 particles, particulate matter with diameter less than 2.5 μm, can get into human breathing passages to cause general diseases like cough, while even smaller particles with diameter less than 1 μm may go inside the air sacs which may increase the risk of lung cancer. Removal of airborne nanoparticles has become an urgent task in recent years.

In first part of this study, the feasibility of using monolithic polyimide aerogels as filter media for removal of airborne nanoparticles in air flow was investigated. Polyimide gels were synthesized from chemical reactions between pyromellitic dianhydride (PMDA), 2,2'-dimethylbenzidine (DMBZ), and 1, 3, 5-triaminophenoxylbenzene (TAB) dissolved in a good solvent. The gels were dried via supercritical drying in CO_2 to obtain the aerogels. The porosity of polyimide aerogels was controlled by changing the initial concentration of solids in the solutions from 2.5 wt% to 10 wt%. The resulting aerogels show high porosity （91%-98%), high surface area (473 m^2/g-817 m^2/g), and low bulk density (0.025 g/cm^3-0.12 g/cm^3). High values of nanoparticle filtration efficiency (>99.95%) was obtained for those monoliths with high bulk density (>0.05 g/cm^3). The measurements showed that air permeability of these aerogels were of the order of 10^{-10} m^2. Carbon dioxide and nitrogen adsorption isotherms were used to determine the fraction of micropores, mesopores, and

macropores in total pore volume of these specimens. A strong proportional relationship between the fraction of macropores and the permeability was observed which indicates that the macropores handled air permeability in these aerogel materials, while the mesopores provided high efficiency in nanoparticle filtration.

In second part of this study, polyimide aerogel microparticles were produced by conducting sol-gel reactions in an oil-in-oil emulsion system. This emulsion system was created by dispersing in cyclohexane the droplets of polyimide solutions prepared in dimethylformamide. The resultant PI aerogel microparticles showed mean diameter of 40 µm and surface area of 512 m^2/g.

DEDICATION

This thesis is dedicated to my beloved parents who give their continuous support to me.

ACKNOWLEDGEMETS

I would like to express my deepest appreciate to my advisor Prof. Sadhan C. Jana for his expert guidance and continuous encouragement to complete this work.

My sincere gratitude goes to my group members for their support and suggestions. I am deeply grateful to Dr. Andrew Shinko for his guidance in the beginning of this work. I also would like to express my thanks to Senlong Gu for enlightening discussions.

TABLE OF CONTENTS

Page

LIST OF TABLES x

LIST OF FIGURES xi

CHAPTER

I. INTRODUCTION 1

II. LITERATURE REVIEW 5

2.1 Airborne particles 5

    2.1.1 What are airborne particles? 5

    2.1.2 Threat of airborne particles to human health 6

2.2 Air filtration 7

    2.2.1 Filtration mechanisms 7

    2.2.2 Filtration efficiency and classification of filters 9

2.3 What is an aerogel? 11

2.4 Aerogel filters 13

2.5 Polyimide aerogels 15

2.7 Supercritical Drying process 18

2.8 Aerogel microparticles 21

III. EXPERIMENTAL 23

3.1 Materials 23

3.2 Preparation methods 23

  3.2.1 Preparation of monolithic polyimide aerogel 24

  3.2.2 Preparation of polyimide aerogel microparticles 27

  3.2.2.1 Preparation of PI solution 25

  3.2.2.2 Preparation of PI aerogel microparticles 25

3.3 Characterization 29

  3.3.1 Density and porosity 29

  3.3.2 Morphology 29

  3.3.3 Thermal stability 30

  3.3.4 Spectroscopic analysis 30

  3.3.5 Surface property 30

  3.3.6 Air permeability 31

  3.3.7 Filtration efficiency 33

  3.3.8 Measurement of diameter of PI aerogel microparticles 34

IV. MONOLITHIC POLYIMIDE AEROGELS AS FILTER MEDIA FOR REMOVAL OF AIRBORNE NANOPARTICLES 34

  4.1 Density and porosity 35

  4.2 Thermal stability 37

4.3 Air permeability 38

4.4 Filtration efficiency 40

4.5 Surface property 42

4.6 Morphology 46

4.7 Spectroscopic analysis 49

4.8 Conclusions 50

V. POLYIMIDE AEROGEL MICROPARTICLES PREPARED BY OIL-IN-OIL EMULSION SYSTEM 52

5.1 Morphology 52

5.2 Surface Property 54

5.3 Spectroscopic Analysis 56

5.4 Conclusions 57

VI. CONCLUSIONS 58

REFERENCES 60

LIST OF TABLES

Table Page

2.1 Classification of air filters EN 1822-1:2009. 10

2.2 Porosity, surface area, and average pore diameter of common organic aerogels. [61-65]..13

2.3 Critical properties of common solvents. [83] 20

4.1 Bulk density, skeletal density, diameter shrinkage, and porosity of monolithic PI Aerogels. 36

4.2 Total pore volume, pore volume of micropores, mesopores, macropores and their fraction in PI aerogel monoliths. 45

5.1 Dimeter shrinkage of monolithic PI aerogel and microparticles. 54

5.2 BET surface area and specific pore volume of PI monoliths and microparticles. 56

LIST OF FIGURES

Figure Page

2.1 Scheme of (a) surface filtration and (b) depth filtration. 7

2.2 Scheme of filtration mechanisms. With permission from Ref [41] 8

2.3 Filtration efficiency of fibrous filter with two main mechanisms. With permission from Ref [45] 11

2.4 Permeability of sPS aerogels vs. bulk density. With permission from Ref [18] 14

2.5 Chemical structure of polyimide. 15

2.6 Photos of mechanically strong and flexible PI aerogels. With permission from Ref [71] 16

2.7 Pressure-temperature phase diagram 19

2.8 Autoclave set-up for preparation of PI microparticles. With permission from Ref [30] 21

3.1 Reaction mechanisms of preparation of polyimide. 25

3.2 Scheme of preparation of PI gels. 26

3.3 Images of (a) CO_2 supercritical dryer and (b) PI aerogel... 27

3.4 Schematic representation of preparation of PI aerogel microparticles. 28

3.5 Schematic representation (a) and images (b,c) of Frazier tester. 33

3.6 Schematic image of specimen set up for TSI-8130. 34

4.1 TGA curves for NMP-based PI and DMF-based PI. Scan rate 10℃/min 37

4.2 Representative data of Frazier test 39

4.3 Permeability of PI aerogels vs. bulk density.. 39

4.4 Filtration efficiency of DMF-based PI aerogels 40

4.5 Filtration efficiency of NMP-based PI aerogels 41

4.6 BET Isotherms and pore size distribution of (a) NMP-based PI and (b) DMF-based PI. 43

4.7 BET surface area of PI aerogel monoliths 44

4.8 Schematic image of “open path” in PI aerogels... 44

4.9 Effect of fraction of pores on air permeability of PI aerogels. (a) macropores, (b) micropores, and (c) mesopores...47

4.10 SEM images of (a) inner network structure and (b) upper surface after filtration test of PI aerogels. Air flow direction is shown by arrows. 47

4.11 Upper surface of PI aerogel after passing the particle 100 times. 48

4.12 FTIR spectra of PI-DMF aerogel.. 50

5.1 SEM images of (a) PI aerogel microparticles, (b) network of PI aerogel microparticles, (c) surface of PI aerogel miroparticles and (d) schematic image of effect of interfacial tension on gel network. 53

5.2 BET isotherms of PI aerogel monolith and microparticles.. 54

5.3 Pore size distribution of PI aerogel monolith and microparticles.............................. 55

5.4 FTIR spectra of PI monolith, PI aerogel microparticles and poly(amic acid)............ 56

CHAPTER I

INTRODUCTION

It is widely known that inhaling airborne particles can cause human being respiratory diseases like cough, breathing difficulties, chronic bronchitis, and even cancers. [1-2] The hazard level of airborne particles shows an inverse relationship to their size. For example, particles with diameter of 5.5-9.2 μm will lodge in human nose and throat leading to breathing difficulties while particles smaller than 5.5 μm can get into the breathing passages to cause more severe diseases. The most hazardous particles are those with diameter less than 1 μm which may stay in air sacs and significantly increase the risk of lung cancer. [3]

PM 2.5, defined as the particulate matter with diameter less than 2.5 μm, is used as the Air Quality Index (AQI) to characterize the concentration of inhalable particles in air. [4] According to a report, for cities in developing countries, like Beijing, the PM 2.5 index reached a new high in year of 2015. [5] Dealing with airborne particles has become an urgent task for governments all over the world. An important way to combat the hazards of nanoparticles is filtration. Commercial masks and high efficiency particulate absorption (HEPA) filters made of fiber mats show as high filtration efficiency as 99.95% for removal of PM 2.5. However, it is difficult to find filter products that consistently remove particles with diameter less than 300nm.

The use of porous materials as filter media has been widely investigated. Porous materials offer high pore volume and large internal surface area. [6] In this context, aerogels are a unique class of materials with high porosity (>90 %), extremely low density (<0.02 g/cm^3), and large surface area (1000 m^2/g) [7-9] A large number of aerogel materials were obtained from polymers [10-12], transition metals [13-14], and other composites materials [15-16]. Ahmed et al. [17] produced aerogels containing metal oxides such as CaO and MgO to capture gases that cause pollution of air. Such gasses as CO_2, SO_2, NO_x, and H_2S were efficiently removed through both chemical and physical mechanisms. The use of monolithic aerogels as filter media for nanoparticles was first studied by Kim et al. [18-19] They prepared syndiotactic polystyrene (sPS) aerogels via thermoreversible gelation and supercritical drying. High filtration efficiency (>99.95 %) was obtained when the bulk density of sPS aerogels was at 0.034 g/cm^3. Correspondingly, air permeability of sPS aerogels were found to be in the range of $5.29\text{-}9.74\times10^{-10}$ m^2.

One of the most well-known organic aerogels is polyimide aerogels. These aerogels gained attention for outstanding thermal stability and was first mentioned in 2004. [20] Researchers fabricated polyimide aerogels by chemically reacting aromatic diamines with dianhydrides. In recent years, a variety of dianhydrides and diamines were used in synthesis of PI aerogels such as 3,3',4,4'-benzophenone tetracarboxylic dianhydride (BTDA), 2,2'-dimethylbenzidine (DMBZ), 3,3',4,4'-biphenyltetracarboxylic dianhydride (BPDA) pyromellitic dianhydride (PMDA), 2,2'-dimethylbenzidine (DMBZ) and 4,4'-oxydianiline (ODA). Different crosslinkers were also investigated. Kawagishi et al. [21] used 1, 3, 5-tris (4- aminophenyl) benzene (TAB), a trifunctional amine crosslinker in conjunction with the mixture of dianhydrides and diamines. As a result, the efficiency of crosslinking was substantially improved. Following this work, Meador and co-workers [22] studied mechanical properties of PI aerogels synthesized from select dianhydrides and diamines, also crosslinked with TAB. These researchers discovered that aerogels containing 2,2'-bis(phenoxyphenyl) propane dianhydride (PPDA) experienced shrinkage which enhanced their moduli. These materials endured greater stress at higher strains. PI aerogels with excellent properties find applications in aerospace technologies such as in insulation of aircraft to facilitate entry, descend, and landing (EDL) processes and as acoustic absorbers. [23-25]

The potential of using monolithic polyimide aerogels as filter media for airborne nanoparticles was investigated in this thesis. PI aerogels were synthesized from pyromellitic dianhydride (PMDA), 2,2'-dimethylbenzidine (DMBZ) and the crosslinking agent 1, 3, 5 triaminophenoxylbenzene (TAB). N-methylpyrrolidone (NMP) and dimethyl formamide (DMF) were used as the solvents. Monolithic PI aerogels were obtained via drying of the gels in supercritical CO_2. The resultant PI specimens showed low bulk density (0.025-0.12 g/cm^3) and large surface area (400-800 m^2/g). High nanoparticle filtration efficiency (>99.95%) was obtained using those monoliths when the bulk density was >0.05 g/cm^3. The measurements showed that air permeability of these aerogels were in the order of 10^{-10} m^2. The effect of fraction of the macropores inside PI aerogel monoliths on air permeability was also studied.

It is known that several classes of materials present impressive properties when their dimensions are reduced from centimeter or millimeter to micrometer or even nanometer. Related applications are found in fields like energy [26] and medicine. [27] In this research, similar concepts were persued via fabrication of PI aerogel microparticles.

The aerogel microparticles were fabricated through two traditional methods. [28-29] In Method I, the micrometer-sized droplets of aqueous polymer solution were created by spray nozzle. [28] Droplets were frozen in liquid nitrogen and freeze-dried to convert them to aerogel. In Method II, micrometer-sized polymer sol were produced in water-in-oil emulsion systems, the sol was allowed to gel, and the gel particles were dried under supercritical condition to obtain aerogel microparticles. [29] In both methods, the aqueous solutions of gel precursors were required. However, for moisture-sensitive polymeric precursors such as polyimides, the above two methods are not suitable. Kwon and co-workers [30] prepared polyimide aerogel microparticles through curing of precursor poly(amic acid) by dispersing in solvents. A special autoclave set-up was needed for curing and the whole procedure lasted over 4 hours at high temperature. A more user-friendly process was developed in this work for synthesis of PI aerogel microparticles via oil-in-oil emulsion process.

In Chapter V of this thesis, a new method of preparation of PI aerogel microparticles is presented. In this method, the sol-gel process was carried out in oil-in-oil emulsion system. The micrometer-sized droplets of PI in DMF solution were dispersed in cyclohexane. Two nonionic surfactants SPAN 85 and Hypermer^{TM} 1599 were used to stabilize the emulsion system. The differences of surface properties and pore structures of PI aerogel microparticles and monolithic PI aerogels are discussed in Chapter V.

CHAPTER II

LITERATURE REVIEW

2.1 Airborne particles

Airborne particles are generated from both natural and fictitious sources and they are considered as main air pollutants.

2.1.1 What are airborne particles?

Airborne particles are microscopic solid or liquid matter suspended in the atmosphere which are regarded as significant pollutants. [2] PM 2.5 is defined as particulate matter with a diameter less than 2.5 μm. Nowadays, as a significant Air Quality Index (AQI), PM 2.5 in developing countries has become a frequently-used headline in news all over the world. According to local record, in year of 2015, average PM 2.5 index in Beijing reached a new high. [5] These particles in atmosphere are generated from both natural and fictitious sources. Some particulate matters can be released by atmospheric conversion reactions, volcanos, dust storms, and natural fires on grassland. Meanwhile, some other anthropogenic particles are generated by burning of fossil fuel in vehicles and various industrial processes. [31] For example, large amounts of particulate pollutants are present in the form of carbon black fillers used in rubber industry. Smaller particles with nanometric diameter may also be produced and released to atmosphere from these sources.

2.1.2 Threat of airborne particles to human health

It is widely accepted that airborne particles are extremely hazardous to human health and the hazard levels of these particles have an inverse relationship to particle size. In terms of size, particulate matters are classified as coarse particles (>1 μm), fine particles (<1 μm), and ultrafine particles (<0.1 μm). [3] [32-33] Coarse particles with diameter 5.5-9.2 μm lodge in nose and throat and cause uncomfortable breathing while those with diameter less than 5.5 μm may get into the breathing passages to cause diseases like cough. The situation becomes more dangerous in the case of fine and ultrafine particles, due to their ability to penetrate into human breathing passages. Fine and ultrafine particles can get into air sacs in humans' lung which significantly increase the risk of lung cancer. [3] Apart from the ability in penetration, pathogen capacity of these particles is considered to be much stronger than the coarse ones. The size of most pathogens is in the range of 0.02 to 2 μm. Pathogens which cause common cold are coronavirus (0.11 μm), echovirus (0.028 nm), rhinovirus (0.023 μm), reovirus (0.075 μm) and adenovirus (0.08 μm). Pneumonia is caused by scyntical virus with diameter of 0.22 μm. Influenza (0.1 μm) and parainfluenza (0.22 μm) are responsible for flue. Larger pathogens such as micromonospora faeni (1 μm) may cause Farmer's Lung disease. [34] These pathogens can be attached on aerosols released by coughing, sneezing, and even talking. A report from World Health Organization (WHO) indicates that 7 million people died in 2012 due to exposure to air pollutants. [35] In view of this, dealing with airborne particles has become an urgent task not only for health of ourselves but also for future generation.

2.2 Air filtration

So far, filtration is considered to be the most efficient way to remove airborne particles and to purify air.

2.2.1 Filtration mechanisms

Filtration is defined as an operation used for separation of solids from liquid or gaseous fluids by filter media. A filter medium is designed so that the fluids can go through it but oversized solids are retained. Nowadays, large size air filters are widely used in specific areas like hospitals to maintain indoor air quality. On the other hand, commercial masks are frequently used to counter high PM2.5 index of outdoor air. In last several decades, companies like 3M developed various series of respiratory masks which can efficiently protect human body from breathing airborne particles. [36]

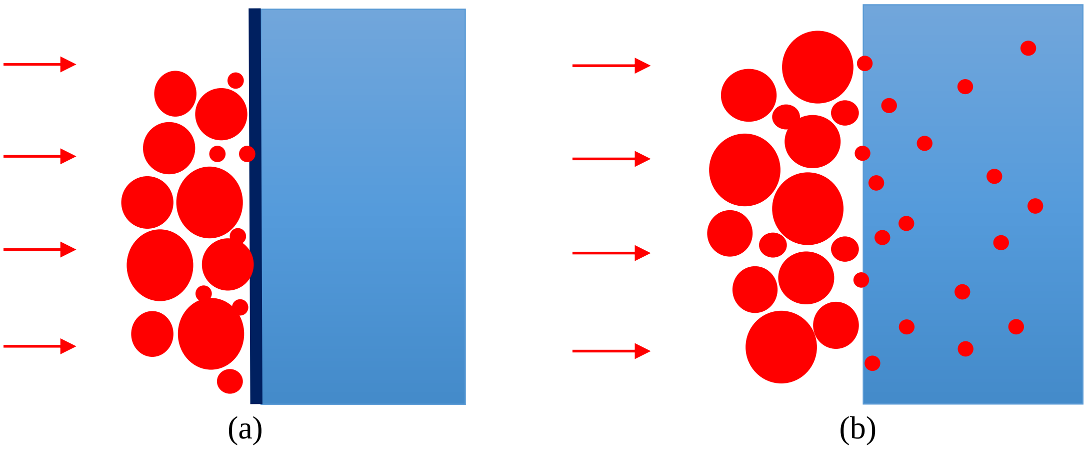

Figure 2.1 Scheme of (a) surface filtration and (b) depth filtration.

In terms of filtration modes, filtration of particles can be divided into surface filtration and depth filtration. [37-38] Figure 2.1 illustrates the scheme of these filtration modes. In surface filtration, solids carried by the fluids are captured by a dense layer at the surface of the filter media. Correspondingly, depth filtration occurs when small particles can get through the filter surface but are captured by the inner granular or fibrous structure of the filter media. [39-40] The commercial masks fabricated from fiber mats also experience surface filtration and depth filtration modes.

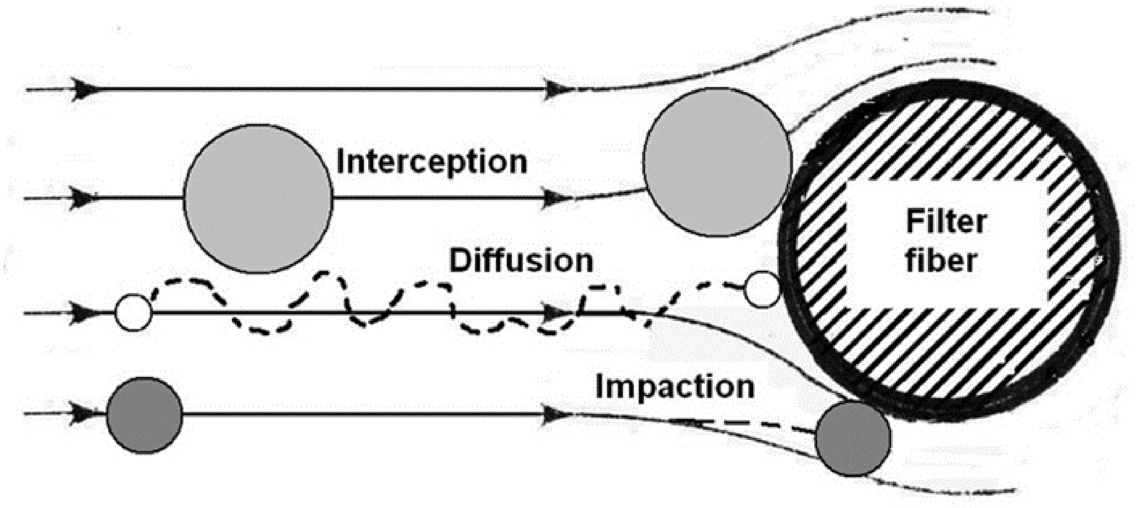

Figure 2.2 Scheme of filtration mechanisms. With permission from Ref [41]

There exists a total of five mechanisms of filtration – (1) direct interception, (2) inertial impaction, (3) diffusional deposition, (4) gravitational settling, and (5) electrostatic forces. [41] The scheme in Figure 2.2 show the modes of direct interception, inertial impaction, and diffusional deposition. Direct interception is a primary mechanism of filtration for capture of large particles. In direct interception, particles with diameter bigger than 1 µm follow the streamlines and are captured when they come in contact with the filter. Smaller particles with diameter less than 1 µm may deviate from the streamlines and are stopped when getting close to the filter media due to inertia. This mechanism is called inertial impaction. Diffusional deposition relies on Brownian motion of ultrafine particles with diameter less than 0.1 µm. In case of gravitational settling, solids are captured in a filter media by gravitational forces. The mechanism of gravitational settling is not suitable for capture of airborne particles as gravitational forces on these particles are too small. Charged particles can be efficiently captured with electrostatic force when passing through filter media. This mechanism is considered significant for removal of ultrafine particles.

For fiber-based filters, direct interception, inertial impaction, and diffusional deposition are three main mechanisms used for capture of airborne particles. [39] [42]

2.2.2 Filtration efficiency and classification of filters

Filtration efficiency is defined as the fraction of particles that remain in the filter media out of the total number of incident particles. Equation (1) illustrates how filtration efficiency(E) is calculated.

$$E = \frac{N_A - N_B}{N_A} \tag{1}$$

In equation (1), E, N_A, and N_B respectively correspond to filtration efficiency, number of incident particles, and number of particles that go through the filter. Penetration (P) is calculated from filtration efficiency(E) by equation (2).

$$P = 1 - E \tag{2}$$

Table 2.1 shows the classification of filters adopted by European Norm EN 1822-1:2009. This classification is widely used by both industrial and academic fields as standard for filter performance. E10-12 in Table 2.1 stands for Efficiency Particulate Air filters

(EPA). H13-14 refers to High Efficiency Particulate Air filters (HEPA) and U15-17 refers to Ultra Low Penetration Air filters (ULPA).

Most HEPA filters are fabricated from glass fibers with diameters 0.5-2 µm. [43-44] Kowalski et al. [45] estimated the effect of particle size on filtration efficiency as shown in Figure 2.3. From this figure, we can see that the efficiency of direct interception increases with an increase of the size of particles. However, the efficiency of diffusional deposition deceases with an increase of particle size. As a result, there exists a particle size

Table 2.1 Classification of air filters EN 1822-1:2009.

Filter Class	Collection Efficiency %	Penetration %
E10	85	15
E11	95	5
E12	99.5	0.5
H13	99.95	0.05
H14	99.995	0.005
U15	99.9995	0.0005
U16	99.99995	0.00005
U17	99.999995	0.000005

around 0.2 µm for a minimum of total filtration efficiency. Correspondingly, HEPA filters can usually have high filtration efficiency of 99.95% for removal of particles with diameter of 0.3 µm. Current literature about air filters for removal of airborne nanoparticles with diameter smaller than 300 nm is scarce.

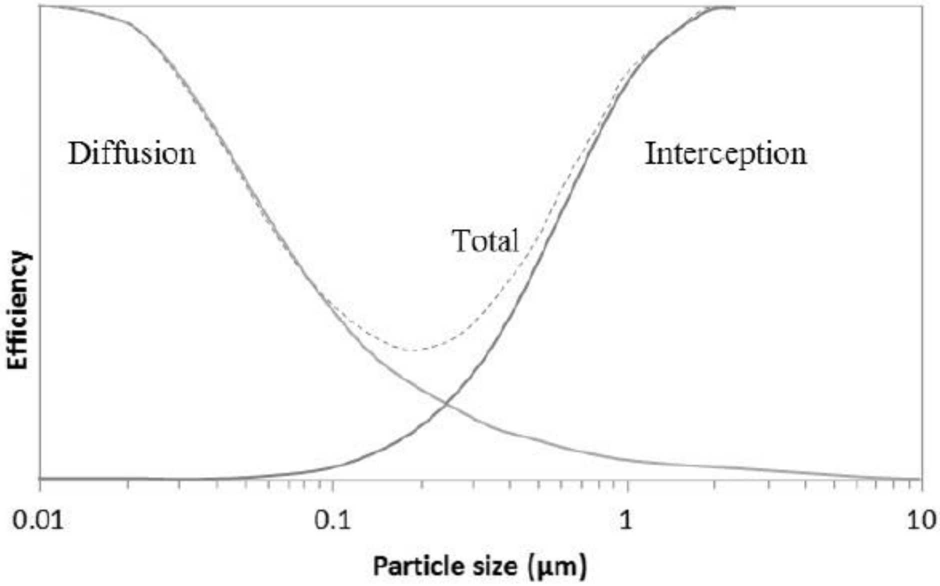

Figure 2.3 Filtration efficiency of fibrous filter with two main mechanisms. With permission from Ref [45].

2.3 What is an aerogel?

Aerogels are ultralight, highly porous materials derived from gels, in which the liquid component is replaced with a gas. With a large number of outstanding properties, such as extremely low density (~3 mg/cm^3), high porosity (>98%), large surface area (~1000 m^2/g), and low thermal conductivity (~0.004 W/m·K), aerogels are attracting interest from both academic and industrial fields. [7-9] Plenty of commercial applications of synthetic aerogels are found such as in architectural and appliance insulation [7] [46], as catalysts [47], as filters [17], and as nanoparticle detectors [25].

The first aerogels were reported in 1931 by Kistler and his co-worker Charles Learned. [48] They prepared gels in a suitable solvent and then replaced the solvent with another liquid of low critical temperature. The liquid inside the gel was converted into gas as the temperature was increased beyond the critical point. As a result, the gel drying occurred without the effect of surface tension. In this way, they successfully produced aerogels of silica, cellulose, alumina, and other materials.

Aerogels have been reported for silica [49-53], polymers [54-56], transition metals [13-14] and hybrid materials [15-16]. Silica aerogels received much focus by researchers since the 1980's due to some of impressive properties such as low density (0.003 g/cm^3), low thermal conductivity (0.005 W/m·K), low index of refraction (~1.05) and high surface area (1000 m^2/g). [57] Kim et al. [58] investigated thermal insulation properties of these materials and drew conclusion that nano-porous structures as well as extremely high surface area of aerogels were responsible for very low thermal conductivity. Inorganic aerogels such as alumina aerogels were prepared and studied for specific catalytic effects. Mizushima, Yasuyuki, and Hori [59] synthesized catalytic metal-supported alumina aerogels for catalysis of methane combustion reactions. The first organic aerogel was prepared by Pekala [60] in 1987 using resorcinol and formaldehyde. The resultant product of the condensation reactions between resorcinol and formaldehyde yielded a network structure. After supercritical drying, resorcinol formaldehyde aerogels were obtained. Since then, a large variety of organic aerogels were produced such as polybenzoxazine [61], polyurethane [62-63], polyurea [63], etc. Table 2.2 includes porosity, surface area, and average pore diameter of some common organic aerogels.

Table 2.2 Porosity, surface area, and average pore diameter of common organic aerogels. [61-65]

Organic aerogels	Porosity (%)	Surface area (m^2/g)	Average pore diameter (nm)
Resorcinol formaldehyde	80-94	400-900	<50
Polyimide	90-98	500-1000	15-30
δ-form syndiotactic polystyrene	85-94	200-300	100-300
Polyurethane	71-80	50-170	30-43
Polyurea	79-86	100-300	9-16
Polybenzoxazine	60-90	40-80	30-40

2.4 Aerogel filters

The use of porous materials as filter media is widely studied due to their advantages like high pore volume and large internal surface area. [7] Aerogels, as they meet the above properties, are considered as effective filter media. A theoretical study on use of aerogels as filter media was first reported in 1989. [66] Researchers used quality factor to compare the performance of aerogels and other filter materials like fiber mats. The result of this study by Cooper [66] indicated that aerogels could perform as well as traditional filters or even better theoretically. Ahmed et al. [17] produced aerogels containing metal oxides such as CaO and MgO to capture the gases that pollute air. The gases CO_2, SO_2, NO_x, and H_2S were efficiently removed through both chemical and physical mechanisms.

Apart from filtration efficiency, air permeability also defines the ability of porous material to serve as filter media. Air permeability of several types of aerogels have been reported. Permeability of carbon aerogels measured by Kong et al. [67] was found to be in the range of 10^{-14} to 10^{-16} m^2. Monolithic silica aerogels with higher porosity than carbon aerogels show permeability in the order of 10^{-12} m^2. [68]

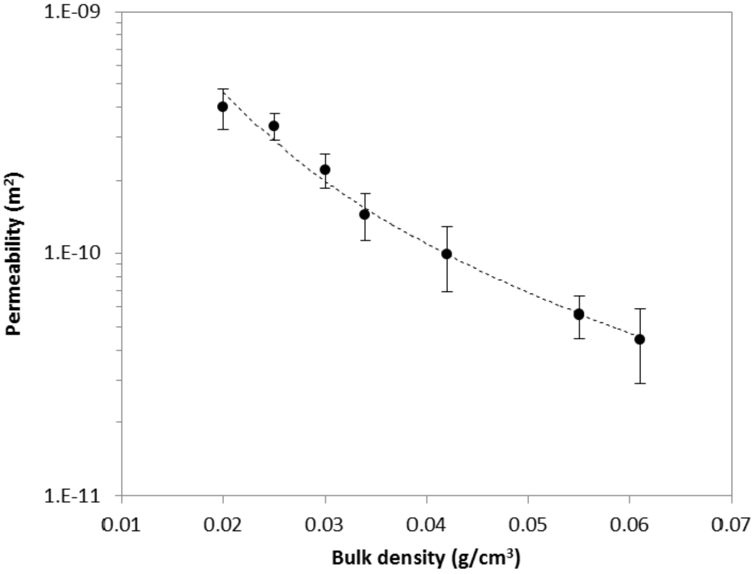

Figure 2.4 Permeability of sPS aerogels vs. bulk density. With permission from Ref [18]

Despite earlier reports, literature on the use of monolithic aerogels as filters for removal of airborne nanoparticles is scarce. The potential of using monolithic aerogels as filters for nanoparticles was first studied by Kim et al. [18-19] They prepared syndiotactic polystyrene (sPS) aerogels via thermoreversible gelation and supercritical drying. High filtration efficiency (>99.95 %) was obtained when bulk density of sPS aerogels was 0.034 g/cm^3 or higher. The values of air permeability followed a power law relationship with bulk density of aerogel specimens as shown in Figure 2.4. The role of mesopore volume fraction in aerogel monoliths in achieving high efficiency airborne nanoparticle filtration was also studied.

2.5 Polyimide aerogels

Among organic aerogels, polyimide aerogels are widely studied because of good mechanical properties and high thermal stability. Polyimide aerogels were first mentioned in 2004. [20] Researchers fabricated polyimide aerogels using a combination of aromatic diamines and dianhydrides. These aerogels were then pyrolyzed to obtain carbon aerogels with ultrahigh surface areas. The polyimide aerogels synthesized via this route lacked physical crosslinking present in other aerogels. To solve this problem, Kawagishi et al. [21] prepared polyimide aerogels with diamines, dianhydrides, and 1, 3, 5-tris (4- aminophenyl) benzene (TAB), the latter is a trifunctional amine crosslinker. The imide structures resulted from thermal imidization at 180 ℃. Figure 2.5 illustrates the chemical structure of polyimide network with 60 repeat units.

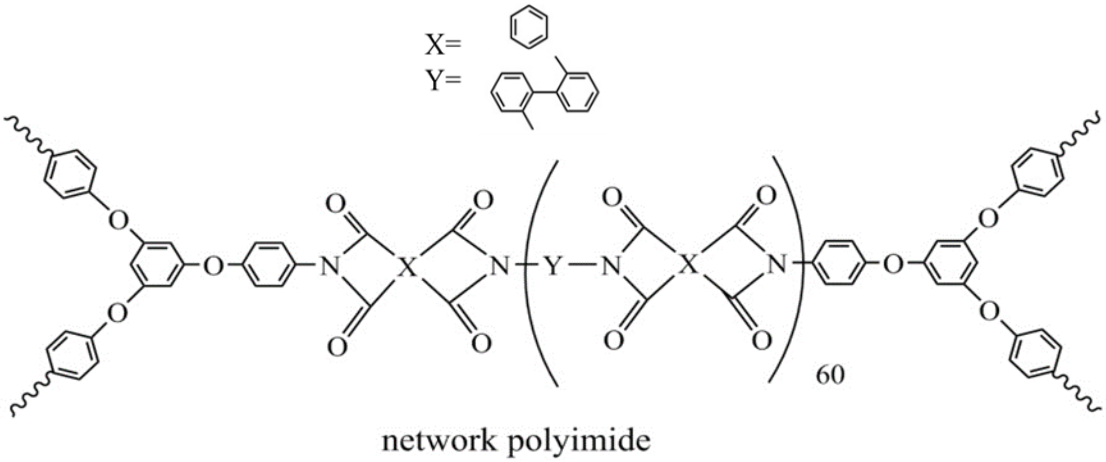

Figure 2.5 Chemical structure of polyimide.

Later, Meador and co-workers [69] produced high crosslink density polyimide gels using three types of polar aprotic solvents: N-methylpyrrolidinone (NMP), dimethyl formamide (DMF), and dimethyl acetamide (DMAC). Gels were heated at 115 °C for 8.5 hours to finish imidization. The gels were then kept in acetone to exchange the solvents with acetone which is miscible with liquid carbon dioxide. After conducting solvent exchange several times, gels were dried in supercritical CO_2. The results illustrated that PI aerogels produced in NMP had the narrowest pore size distribution and the highest surface areas (410 m^2/g). Meador et al. [70] later synthesized polyimide gels using a variety of diamines and dianhydrides including 3,3',4,4'-benzophenone tetracarboxylic dianhydride (BTDA), 2,2'-dimethylbenzidine (DMBZ), 3,3',4,4'-biphenyltetracarboxylic dianhydride (BPDA) pyromellitic dianhydride (PMDA), 2,2'-dimethylbenzidine (DMBZ) and 4,4'-oxydianiline (ODA). The resultant aerogels showed high surface areas (200-410 m^2/g) and low densities (15-32 mg/cm^3).

Figure 2.6 Photos of mechanically strong and flexible PI aerogels. With permission from Ref [71].

Meador and co-workers [22] also studied mechanical properties of select dianhydrides and diamines crosslinked with TAB. These researchers discovered that aerogels containing PPDA showed high shrinkage which enhanced the moduli and endured higher stress at higher strains than other polyimide aerogels studied by these authors. On the other hand, the DMBZ-containing aerogels provided lower bulk densities and larger porosity. In 2012, Meador et al. [71] prepared mechanically strong, flexible polyimide aerogels using TAB as the crosslinker. The PI aerogels fabricated from 4,4'-oxydianiline (ODA) and 2,2'-dimethylbenzidine (DMBZ) were continuously produced in the form thin films using roll-to-roll machine. These PI aerogel thin films with tensile strength of 4-9 MPa were strong enough to be rolled or folded and then could recover quickly. As shown in Figure 2.6, the PI aerogel monolith was able to withstand the mass of a whole vehicle. Additionally, these PI aerogels had outstanding thermal stability. There was almost no weight loss until temperature was raised up to 450 ℃.

Leventis et al. [72] employed a solution of PMDA with either methylene di-p-phenyldiisocyanate (MDI) or methylene dianiline (MDA) to produce polyimide aerogels without a crosslinker. Acetic anhydride and pyridine were used as the imidization agents to obtain the imide groups. However, chemical imidization turned out to be incomplete. The materials lost around 5% to 7% weight at temperatures much lower than the normal decomposition temperature of PI aerogels. The resultant aerogels had surface area of 430 m^2/g. Later, Leventis and co-workers [73] synthesized bisnadimide using nadic anhydride, MDA, and cyclopentadiene. Bisnadimide was then polymerized through ring opening metathesis polymerization (ROMP) in the presence of second generation Grubb’s catalyst.

PI aerogels fabricated in this method had obviously high values of shrinkage (~30%). However, relatively low density aerogels (0.134 g/cm^3) had high surface areas (632 m^2/g).

Tailoring of properties of monolithic PI aerogels with fillers was also attempted. Vivod et al. [23] produced BPDA-ODA and BTDA-ODA based PI aerogels filled with carbon nanofibers. BPDA-ODA based aerogels showed an obvious increase of toughness and flexibility. Nguyen et al. [74] incorporated cellulose nanocrystals (CNCs) into PI aerogels. CNCs were added into dianhydride and diamine solutions prior to reactions. As a result, the mechanical properties of PI aerogels were enhanced due to good interactions between the PI network and CNCs.

Excellent properties of PI aerogels find applications in aerospace technologies such as in insulation of aircraft, facilitating entry, descend and landing (EDL) processes and acoustic absorbers. [23-25] Another important application of PI was discovered in the field of shape memory polymers (SMPs). Koerner et al. [75] investigated polyimides with shape memory properties. They synthesized PI by using hexafluoropropane dianhydride (6FDA) and 1,3-bis(3-aminophenoxy)benzene (ABP). The resultant PI illustrated both high shape fixity (~99.7%) and high shape recovery (99.5%). The apparent reason for such shape memory properties was sharp transition of PI from glassy to rubbery state.

2.7 Supercritical drying process

Aerogels are produced by drying wet gels under supercritical condition. The drying process has significant effect on the properties of aerogels. The capillary force was developed during evaporation of the liquid inside the pores of the gels which may destroy the structure and cause cracks. There are three main methods [76-77] used for drying of gels:

(1) Freeze drying – requires bypassing the triple point.

(2) Evaporation – necessitates cross path of the liquid-gas equilibrium curve.

(3) Supercritical drying – requires bypassing the supercritical point.

Generally, freeze drying results in cracked specimens or even powders. [78] Evaporation without specific treatment during aging leads to samples with high density. [79] Strategies to avoid cracking of gels during drying process have been investigated. [80-82] Parameters like pore size, aging time of gels, and hydrophobic treatment are considered to be the factors that control drying. Crack-free xerogels can be obtained by controlling these parameters but large diameter shrinkage cannot be prevented.

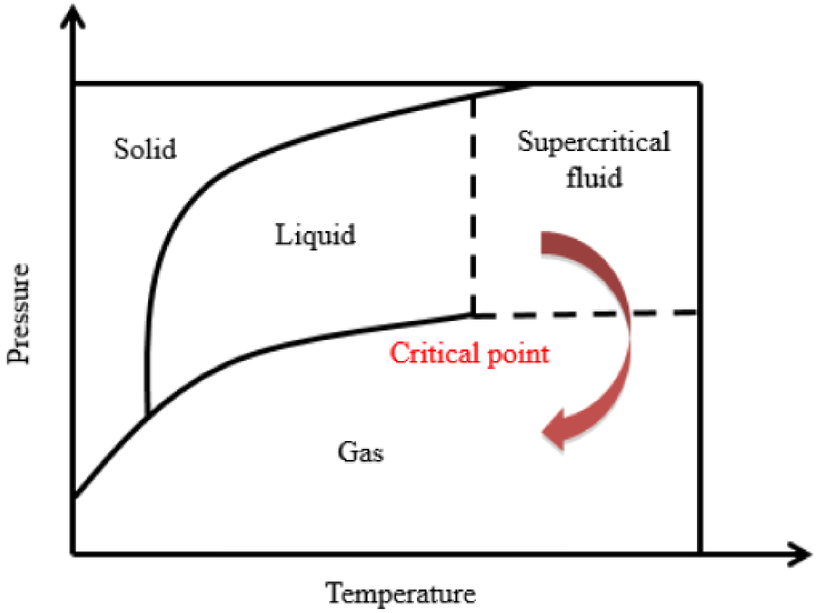

Figure 2.7 Pressure-temperature phase diagram.

In supercritical drying, liquid components of wet gels are transferred into supercritical state where liquid surface tension can be avoided. As a result, capillary stress can be reduced to a minimum. Figure 2.7 shows the mechanism of supercritical drying. The solvent can be transferred into gaseous state without crossing the phase boundary of liquid and gas. This process usually requires high temperature and high pressure. Table 2.3 illustrates the critical properties of common solvents.

Table 2.3 Critical properties of common solvents. [83]

Solvent	T_C (℃)	P_C （MPa）
Methanol	240	7.9
Ethanol	243	6.3
Acetone	235	4.7
H_2O	374	22.1
CO_2	31	7.3
Cyclohexane	279	4.07

As shown in Table 2.3, the critical temperature of CO_2 is relatively low compared with other solvents. As a result, liquid CO_2 is widely used in supercritical drying process due to safety and low energy needs. However, the price of liquid CO_2 and the relatively long time needed for the drying step makes CO_2 supercritical drying still a costly process.

2.8 Aerogel microparticles

It is known that materials present impressive properties when their dimensions are reduced from centimeter or millimeter to micrometer to even nanometer. Related applications are found in the fields of energy [26] and medicine [27].

Aerogel microparticles fabrication follow two traditional methods. [28-29] In Method I, micrometer-size droplets of aqueous polymer solution were created by spray nozzle. Then these droplets were then frozen in liquid nitrogen followed by freeze-drying to form the aerogel micropartiles. [28] In method II, micrometer-size polymer gels were produced in water-in-oil emulsion system. [29] The aerogel microparticles were obtained by supercritical drying. In both methods, the aqueous solutions of gel precursors are required. However, for moisture-sensitive polymeric precursors, such as polyimides, these two methods are not suitable.

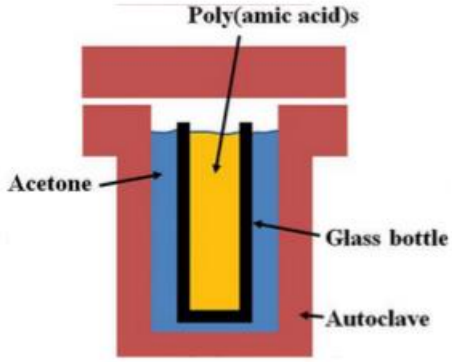

Figure 2.8 Autoclave set-up for preparation of PI microparticles. With permission from Ref [30]

Kwon and co-workers [30] prepared polyimide aerogel microparticles through curing of precursor poly(amic acid) within the solvents. A special autoclave set-up as shown in Figure 2.8 was used for curing. The poly(amic acid) solution was placed in glass bottle that was then placed in the autoclave. The space between the glass bottle and autoclave was filled with acetone. As the temperature increased from 150 ℃ to 250 ℃, PI aerogel microparticles were fabricated. The whole procedure lasted over 4 hours.

CHAPTER III

EXPERIMENTAL

This chapter lists materials used in this study and describes detailed procedures for preparation monolithic polyimide aerogels and polyimide aerogel microparticles. Additionally, characterization methods used in this study are described.

3.1 Materials

Pyromellitic dianhydride (PMDA) was purchased from Alfa-Aesar and 2,2′-dimethylbenzidine (DMBZ) was purchased from Shanghai Worldyang Chemical Co., Ltd (Shanghai, China). The chemical crosslinker 1,3,5-tris(4-aminophenoxy)benzene (TAB) was provided by Triton Systems (Chelmsford, MA) as a dull brown powder. SPAN 85, anhydrous N-methylpyrrolidinone (NMP) and anhydrous dimethylformamide (DMF) were obtained from Sigma-Aldrich. Hypermer^{TM} 1599 was provided by Croda Inc (Edison, NJ). Pyridine, acetic anhydride, cyclohexane, and acetone were purchased from Fisher Scientific. All reagents and solvents were used as received.

3.2 Preparation methods

This section introduces the methods used in the preparation of monolithic polyimide aerogels and polyimide aerogel microparticles.

3.2.1 Preparation of monolithic polyimide aerogel

In this study, the amount of solids was accurately calculated according to the weight concentrations of polyimide products in final solutions. Stoichiometric ratio of PMDA and DMBZ was set as 61:60 mole:mole to ensure that the length of repeat unit n was 60. Polyimide solutions with solid weight of 2.5%, 5%, 7.5% and 10% were prepared. Two

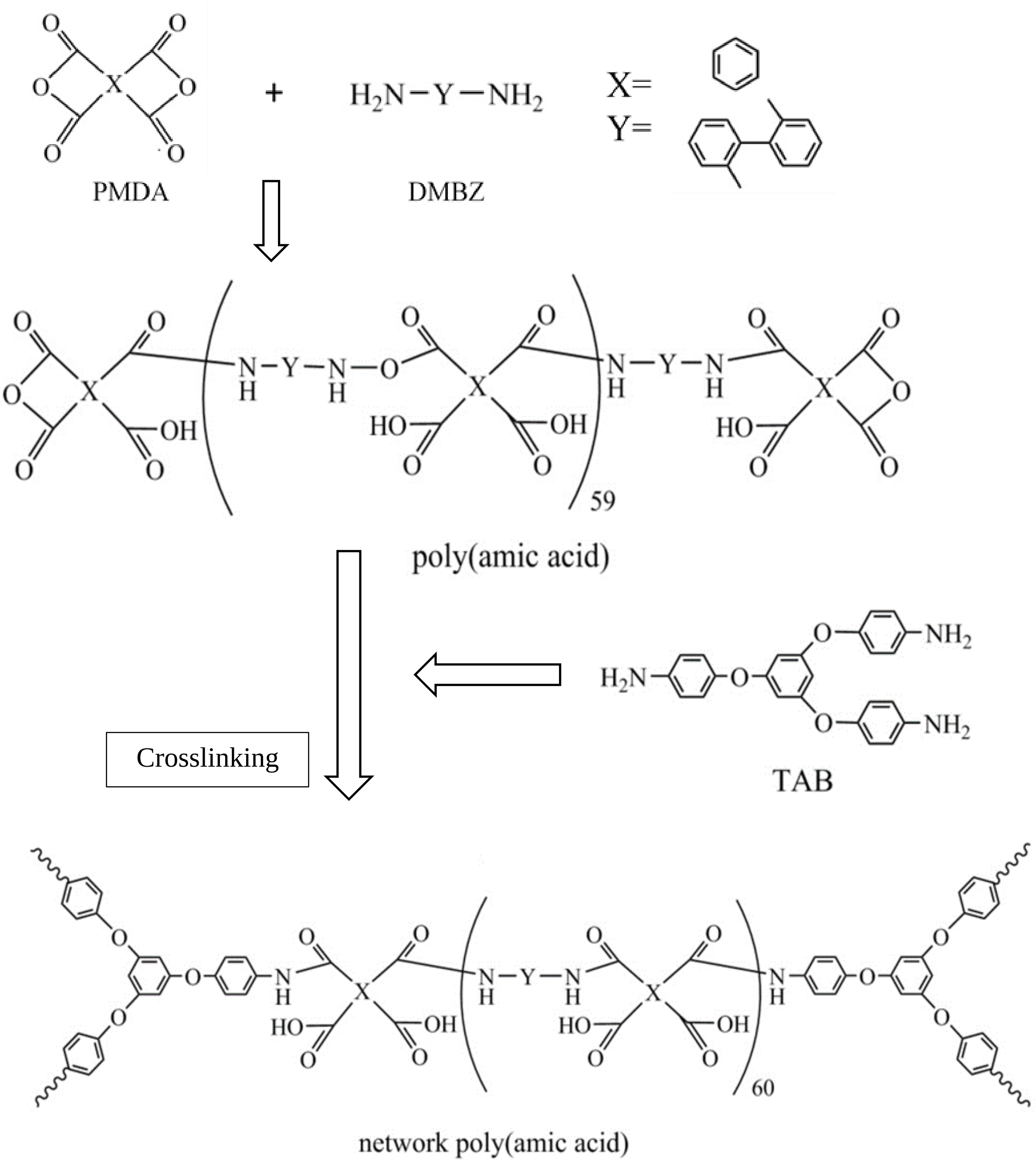

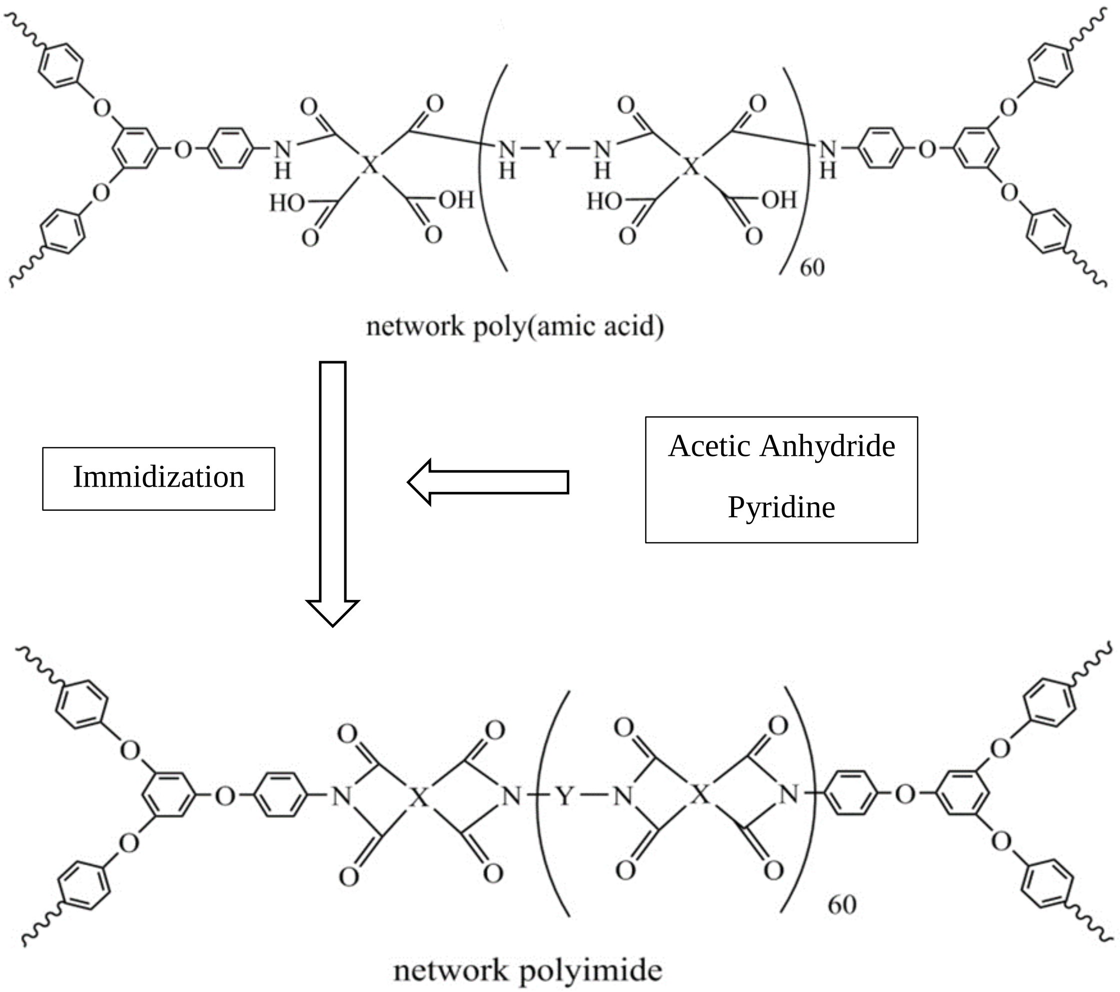

Figure 3.1 Reaction mechanisms of preparation of polyimide.

different solvents, NMP and DMF, were used for comparison of aerogel materials properties. All reactions occurred at room temperature. The scheme of reactions in preparing PI chains is presented in Figure 3.1.

Pyromellitic dianhydride (PMDA) and 2, 2′-dimethylbenzidine (DMBZ) were separately added in the chosen solvent and magnetically stirred at 300 rpm until clear solutions were obtained. The process usually took 5 to 30 minutes depending on the amount of monomers. Then, the dianhydride and diamine solutions were mixed with each other to obtain a translucent and homogenous mixture. The mixture contained poly (amic acid) oligomers. After another ten minutes of stirring, the solution of trifunctional crosslink agent

1, 3, 5-tris (4- aminophenyl) benzene (TAB) was added into the mixture to form the networks. Acetic anhydride and pyridine which worked as dehydrating agents and reaction catalyst were added to remove water and form imide group. Polyimide solution was poured into a disk shaped mold of diameter of 32 mm to obtain the gel. The gelation times were dependent on the concentration of the solid. For example, a solution with 2.5 wt% solids needed more than three hours while a 10 wt% solution only needed 10 minutes to gel. All gels were kept in molds for 24 hours for aging. Afterwards, the solvent DMF or NMP in polyimide gels were exchanged with acetone six times. Each time, the exchange process took approximately eight hours. Finally, these acetone-filled gels were placed inside the chamber of the supercritical dryer for solvent exchange with liquid CO_2. At the end, the temperature was raised to 50 ℃ and the pressure was raised to over 7.3 MPa to obtain aerogels. A scheme of preparation of PI aerogels is shown in Figure 3.2 and Figure 3.3.

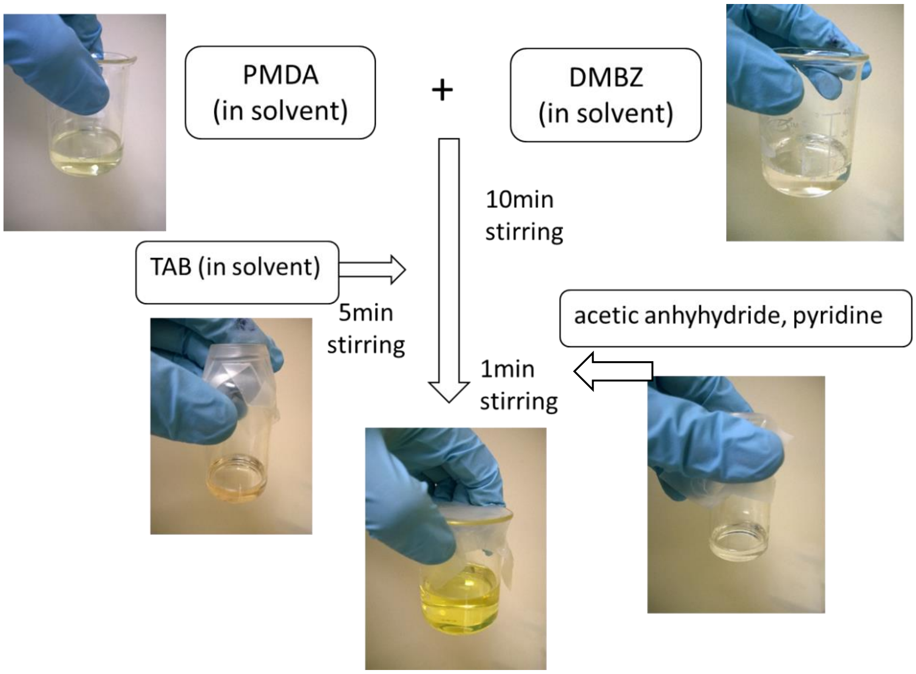

Figure 3.2 Scheme of preparation of PI gels.

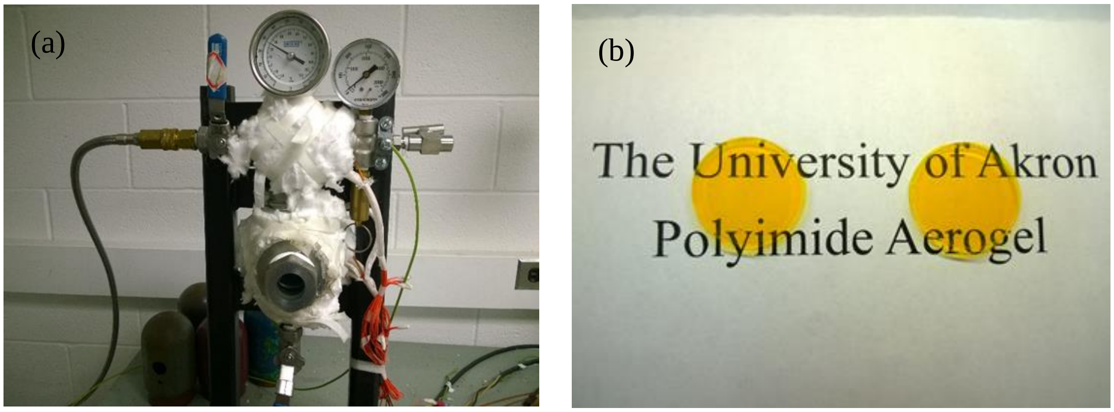

Figure 3.3 Images of (a) CO_2 supercritical dryer and (b) PI aerogel.

The other details are as follows. In order to avoid shrinkage, a gradient in concentration of the exchange solvents was used. The first three times, mixed solvents consisting of original solvent (NMP or DMF) and acetone in volume ratio of 75/25, 50/50 and 25/75 were used. Afterwards, the wet gels were exchanged with 100% acetone.

3.2.2 Preparation of polyimide aerogel microparticles

This section describes how polyimide aerogel microparticles are prepared by oil-in-oil emulsion system.

3.2.2.1 Preparation of PI solution

0.1660 g of PMDA and 0.1590 g of DMBZ were individually dissolved in 4.1 mL of DMF and 5.1 mL of DMF respectively to form homogeneous solutions. PMDA and DMBZ solutions were mixed to produce light yellow, translucent mixtures. A solution of 0.0025 g TAB in 1 mL DMF was then added into the mixture. After 5 minutes of stirring, 0.5757 g acetic anhydride and 0.4925 g pyridine were added drop by drop into this solution. The mixture remained translucent but the color turned to dark yellow.

3.2.2.2 Preparation of PI aerogel microparticles

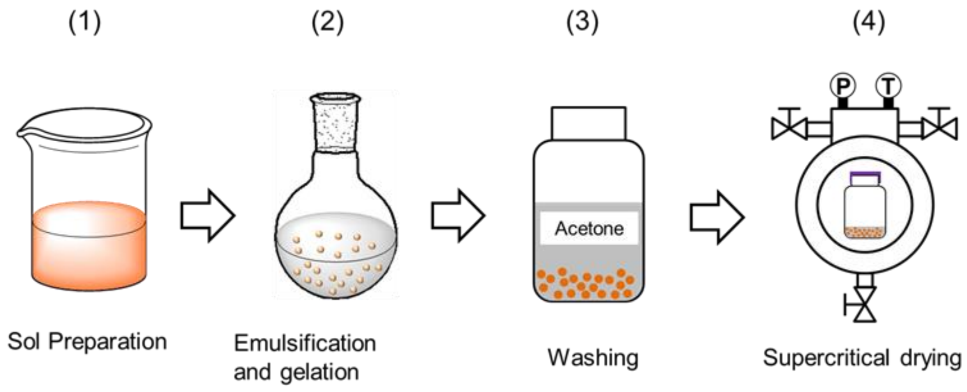

Figure 3.4 Schematic representation of preparation of PI aerogel microparticles.

The preparation process included four steps, as illustrated in Figure 3.4. (1) The sols in DMF were prepared following the procedure described above. (2) 4 mL of sol was dispersed in 32 mL of cyclohexane with SPAN 85 (0.748 g) and Hypermer™ 1599 (0.249 g) dissolved in it to obtain oil-in-oil emulsion. The emulsion was stirred for about 3 h using magnetic stirrer set at 400 rpm to obtain the gel microparticles. (3) The emulsion was poured into acetone and the supernatant was removed to recover the gel microparticles. The gel microparticles were then washed 6 times with acetone in a Thinky® Mixer at 1000 rpm, each wash cycle spanning 5 min to remove the surfactants. (4) The gel microparticles were then dipped in liquid CO_2 to exchange acetone and supercritically dried to obtain aerogel microparticles. The gel microparticles were retained in the container during exchange of acetone with liquid CO_2 and subsequent supercritical drying step by holding the gel microparticles in Kimwipes^{TM} paper membrane. This allowed passage of the exchange liquid but prevented the loss of microparticles from the container.

3.3 Characterization

This section describes the characterization methods used in this work. The parameters used in characterization and the preparation of specimens are also presented.

3.3.1 Density and porosity

The bulk density (ρ_b) of monolithic PI aerogel specimens were directly calculated from the mass and the volume, as equation (3). Skeletal density (ρ_s) was measured by Accupyc 1340 helium pycnometer (Micromeritics Instrument Corp.). Porosity (Π) was obtained from the values of bulk density (ρ_b) and skeletal density (ρ_s) using equation (4). Diameter shrinkage (δ_d) was calculated from the diameter of gels and dried aerogels using equation (5). The total pore volume (V_T) was determined from equation (6).

$$\rho_b = \frac{4m}{\pi d^2 h} \qquad (3)$$

$$\Pi = 100 \times \left(1 - \frac{\rho_b}{\rho_s}\right) \qquad (4)$$

$$\delta_d = 1 - \left(\frac{d}{d_0}\right) \qquad (5)$$

$$V_T = \frac{1}{\rho_b} - \frac{1}{\rho_s} \qquad (6)$$

In equations (3) and (5), m, h, d, and d_0 refer respectively to mass of aerogel specimen, height of aerogel specimen, diameter of aerogel, and diameter of the gel.

3.3.2 Morphology

Morphologies of polyimide aerogels specimen were observed via scanning electron microscope (JEOL JSM5310) at 8 kV. In order to take images of fractures, monolithic PI aerogels were broken off with hands and thin pieces of fracture surface were cut off by a razor blade. The thin pieces were then mounted on an aluminum stub by using adhesive carbon tape. PI aerogel microparticles were carefully poured on the same stub covered by adhesive carbon tape. All specimens were sputter-coated with silver by ISI-5400 Sputter Coater. For monolithic PI aerogels, the images were taken of the internal network structures and the upper surfaces of the specimens collected after filtration tests. For PI aerogel microparticles, the morphologies of the whole particles and the inner network structures were also observed.

3.3.3 Thermal stability

The thermal stability of PI aerogels was studied by thermogravimetric analysis TGA 2050 (TA Instrument, New Castle, DE) under nitrogen flow. Specimens were placed in a platinum pan and heated up to 800℃ with a ramp rate of 10 ºC/min.

3.3.4 Spectroscopic analysis

Infrared (IR) spectra were recorded with a resolution of 1.4 cm^{-1} on a Brucker FT-IR Alpha spectrophotometer using a Platinum ATR accessory. Representative peaks for functional groups were analyzed to ensure the completion of imidization reactions.

3.3.5 Surface property

Micromeritics Tristar II Surface Area Analyzer was used to characterize specific pore volume. Aerogels were weighed and cut into small particles with diameter about 5 mm to fit sample tubes before test. The amount of sample needed was usually no more than 0.05 g. The specimens were subjected to 12-hour degassing at room temperature for the purpose of removing the impurities. Nitrogen adsorption was carried out at 77 K to obtain the specific pore volume of the mesopores (2-50 nm) and carbon dioxide adsorption was conducted at 273 K to obtain the specific pore volume of the micropores (<2 nm). The data from the measurements were analyzed using Brunauer-Emett-Teller (BET) and Barrett-Joyner-Hacienda (BJH) methods to establish a relationship between the relative pressure and the volume of gas adsorbed. [84] The pore volume of macropores (>50 nm) can be obtained using equation (7). The fraction of micropores, mesopores, and macropores in aerogel monoliths were determined by multiplying the porosity with the fraction of these pores in the total pore volume, as is given in equation (8).

$$V_{ma} = V_T - V_{mi} - V_{ms} \tag{7}$$

$$V'_{mi} = \frac{V_{mi}}{V_T} \times \Pi \,; V'_{ms} = \frac{V_{ms}}{V_T} \times \Pi \,; V'_{ma} = \frac{V_{ma}}{V_T} \times \Pi \tag{8}$$

In Equation (7-8), V_T, V_{mi}, V_{ms}, V_{ma}, and Π are respectively the total pore volume, micropore volume, mesopore volume, macropore volume, and the porosity. The corresponding V' values refer to the fraction of these pores in the polyimide aerogel monolith.

3.3.6 Air permeability

Air permeability of polyimide aerogels was obtained from modified Darcy's law, shown in equation (8).

$$Q = \frac{kGA}{\mu}\frac{\Delta P}{L} \tag{8}$$

In equation (8), Q, k, G, A, ΔP, μ and L correspond respectively to volumetric air flow rate, permeability constant, shape factor, cross-sectional area of the face normal to air flow direction, pressure drop, viscosity of air, and the thickness of aerogel specimen. Frazier tester (Frazier Precision Instrument, Hagerstown, MD) was used here to obtain the values of air permeability constant *k*. Figure 3.5 illustrates the schematic image of set up for Frazier test. Polyimide aerogel specimens were placed at the center of the base plate which had a hole of diameter 5 mm. The sample holder had a central hole with diameter 30 mm for the air flow. Vacuum grease was used to get rid of the gap between the sample holder, the base plate, and the aerogel specimen. Afterwards, this specimen set up was placed on the Frazier permeability tester which had a pressure gauge and a vacuum pump attached to the tester. By controlling the power of vacuum pump, different values of pressure drop ΔP as well as the volumetric flow rate Q were recorded. The values of permeability constant k were calculated from Q vs. ΔP data with the help of equation (8). Since the size of central holes on sample holder and the base plate were different for some tests, the shape factor G was used to accommodate such differences. [85] The values of shape factor G used in this work ranges from 1.5 to 3.

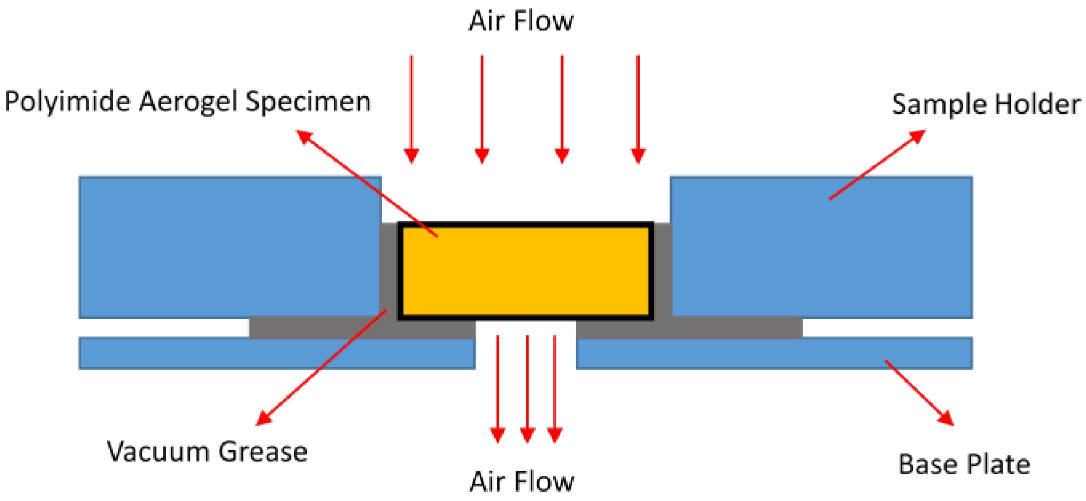

(a)

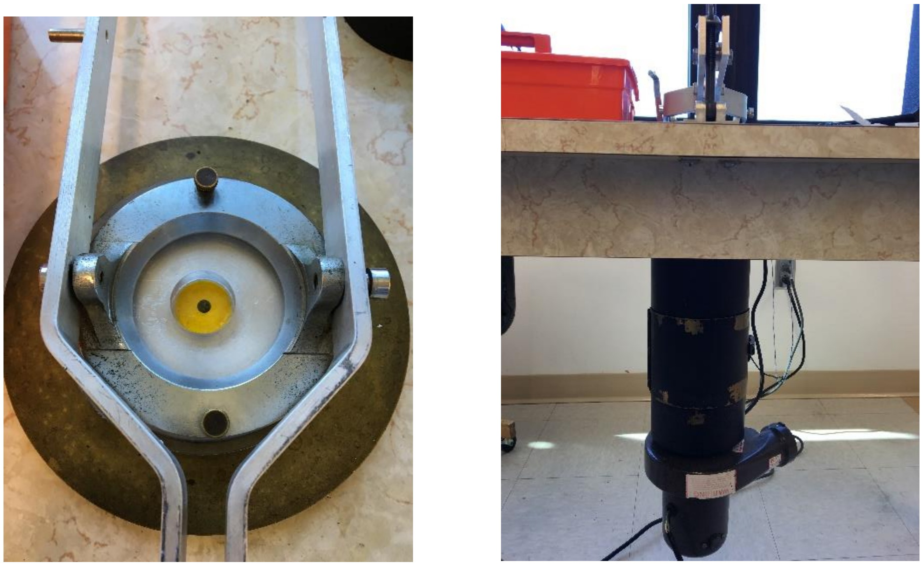

(b) (c)

Figure 3.5 Schematic representation (a) and images (b, c) of Frazier tester.

3.3.7 Filtration efficiency

Filtration efficiency was measured using TSI-8130 filter tester (TSI Inc., Shoreview, MN). The instrument is able to generate sodium chloride nanoparticles with average diameters of 75 nm in air flow. [85] The aerogel specimen was placed in the sample holder with 30 mm diameter on a wide-mesh metal net supporting the specimen placed at the bottom of the holder. Two O-rings were placed tightly along the edge of the aerogel samples to avoid nanoparticles going through the gap shown in Figure 3.6. As shown in equation (9), filtration efficiency was easily obtained from the fraction of nanoparticles not captured by the aerogel monoliths. The maximum of filtration efficiency that can be measured by the instrument is 99.999%. Air flow rate in this test was controlled at 20 L/min.

$$\mathrm{E} = \frac{N_A - N_B}{N_A} \qquad (9)$$

In equation (9), E, N_A, N_B respectively correspond to filtration efficiency, the number of incident particles, and the number of output particles.

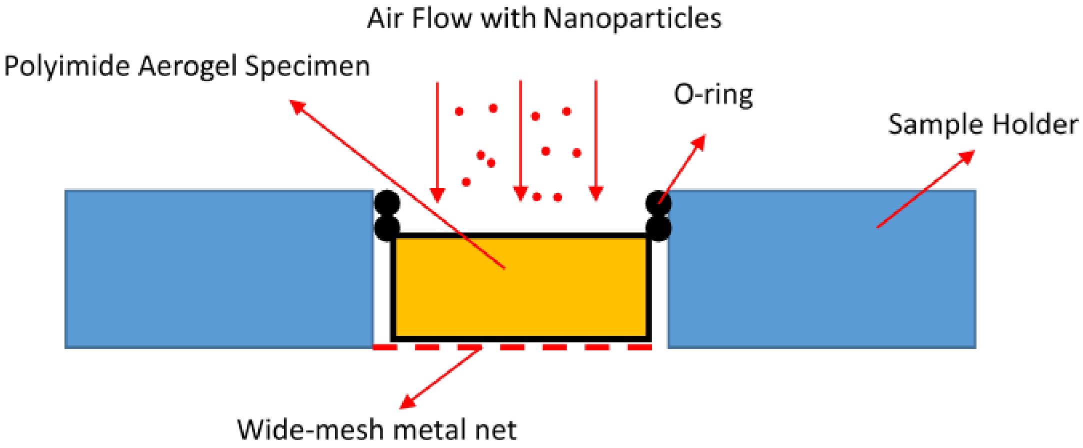

Figure 3.6 Schematic image of specimen set up for TSI-8130.

3.3.8 Measurement of diameter of PI aerogel microparticles

The open source software ImageJ was used for measuring the diameter of microparticles. For this purpose, optical microscope images of the gels and SEM images of the aerogels were used. At least 100 microparticles were considered in each case. The diameter shrinkage of the microparticles was determined from the diameter of gel microparticles and the aerogel microparticles. Optical microscope (OM; OLYMPUS BX51) was used to measure the diameter of gel microparticles.

CHAPTER IV

MONOLITHIC POLYIMIDE AEROGELS AS FILTER MEDIA FOR REMOVAL OF AIRBORNE NANOPARTICLES

This chapter presents characterization results on monolithic PI aerogels and their potential usage as air filters for removal of airborne nanoparticles.

4.1 Density and porosity

The values of bulk density, skeletal density, diameter shrinkage, and porosity are listed in Table 4.1. The average values listed in the table were calculated from at least three measurements. The bulk density increased from 0.025 g/cm^3 to 0.121 g/cm^3 with an increase of weight concentration of solids in the initial solution. The skeletal densities, however, did not change much (~1.5%) as the same monomers were used in all experiments. It was reported that skeletal density of polyimide aerogels strongly depended on the types of dianhydrides and diamines. [63] According to previous studies, BTDA-BAPP system shows as low skeletal density as 1.24 g/cm^3 and PMDA-PPDA produces relatively high skeletal density of 1.63 g/cm^3. The data in Table 4.1 show that DMF-based specimens undergo less shrinkage and show lower bulk density than NMP-based ones. This may be due to the different values of surface tension of the two solvents. At 20 ℃, the surface tension of NMP is 40.79 mN/m while that of DMF is 37.10 mN/m. For the same pore diameter, ~9% less surface tension in the case of DMF than NMP also create ~9% less capillary stress. In this context, the specimen 2.5% PI-DMF experienced 20% less shrinkage than the specimen 2.5% PI-NMP. Similarly, the specimen 10% PI-DMF underwent 26% less shrinkage than the specimen 10% PI-NMP. Note that capillary stress during drying is a principal factor responsible for shrinkage of aerogel monoliths. However, considering the above trend of the data, it appears that pore diameter in the sample specimens could be different as well. Less shrinkage in DMF-based aerogels also led to lower bulk densities and higher porosities. Higher porosities contribute to the total pore volume of these materials, which in turn, produce higher air permeability. These will be discussed in a later section of this thesis.

Table 4.1 Bulk density, skeletal density, diameter shrinkage, and porosity of monolithic PI aerogels.

Specimen	Bulk density, ρ_b (g/cm^3)	Skeletal density, ρ_s (g/cm^3)	Diameter shrinkage, δ_d (%)	Porosity, $\boldsymbol{\Pi}$ (%)
2.5% PI-NMP	0.030 ± 0.0021	1.3638	8.12 ± 2.01	98
5.0% PI-NMP	0.058 ± 0.0018	1.3808	13.86 ± 2.88	96
7.5% PI-NMP	0.091 ± 0.0019	1.3829	13.70 ± 3.01	93
10 % PI-NMP	0.121 ± 0.0027	1.4126	13.65 ±2.80	91
2.5% PI-DMF	0.025 ± 0.0011	1.3668	6.47 ± 2.12	98
5.0% PI-DMF	0.051 ± 0.0022	1.3822	7.67 ±2.01	96
7.5% PI-DMF	0.076 ± 0.0023	1.4009	8.83 ± 2.97	95
10 % PI-DMF	0.101 ± 0.0020	1.4288	10.02 ±3.01	93

4.2 Thermal stability

TGA traces of PI aerogel are presented in Figure 4.1. The specimens were heated up to 800 ℃ at a ramp of 10 ℃/min. Both NMP-based and DMF-based PI aerogels started to lose weight above 50 °C but retained more than 90% of specimen weight until the temperature went up to around 500 ℃. Furthermore, the specimens did not experience a noticeable weight loss between 200-250 °C. This confirms that imidization reactions in the specimens were completed. Otherwise, a weight loss event would have been observed in this temperature range due to the loss of water from the amide sites. [67] A highest possible weight loss of 2% for both PI specimens before 300 °C indicates that imidization was either complete or nearly complete.

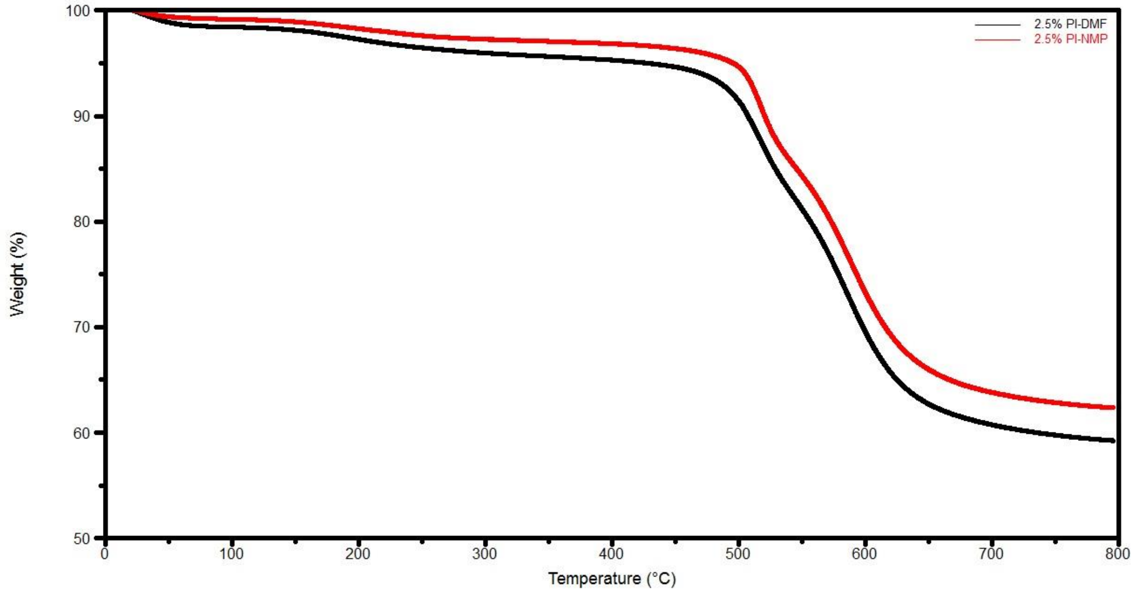

Figure 4.1 TGA curves for NMP-based PI and DMF-based PI. Scan rate 10 °C/min.

4.3 Air permeability

Figure 4.2 shows a representative set of Q vs. ΔP data from Frazier test. The air permeability of specimens was inferred from the slope of Q vs. ΔP curve. The permeability constant k reveals a power-law dependence on bulk density of the specimens as shown in Figure 4.3. A similar power-law relationship was found in the case of δ-form syndiotactic polystyrene (sPS) aerogels by Kim et al. [18] The data in Figure 4.3 indicate that air permeability of polyimide aerogels varied from around 1×10^{-10} m^2 to 4×10^{-10} m^2 which is much higher than the values reported for carbon aerogels (10^{-14} m^2) and similar to the data for δ-form syndiotactic polystyrene (sPS) aerogels. [18] [62] Relatively low porosity (80%) resulted in lower air permeability in the case of carbon aerogels. However, even though the porosity of polyimide aerogels with low solids content can reach 98% which is higher than porosity of fiber mat (60%-90%), the air permeability of those specimens are in the same level with fiber mat filters (10^{-11}-10^{-10} m^2). [86] Skin layers in PI aerogels can account for low values of air permeability. During aging and solvent exchange, the surface of gels come in contact with open air and may develop denser materials. Thus, most of the aerogel materials formed skin layers. Due to this dense skin layer, air permeability of monolithic aerogels could not be higher than what is reported here.

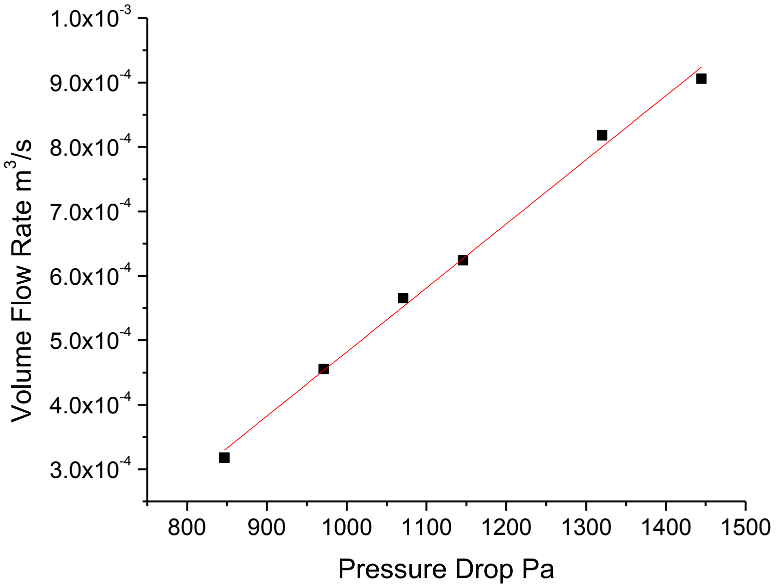

Figure 4.2 Representative data of Frazier test.

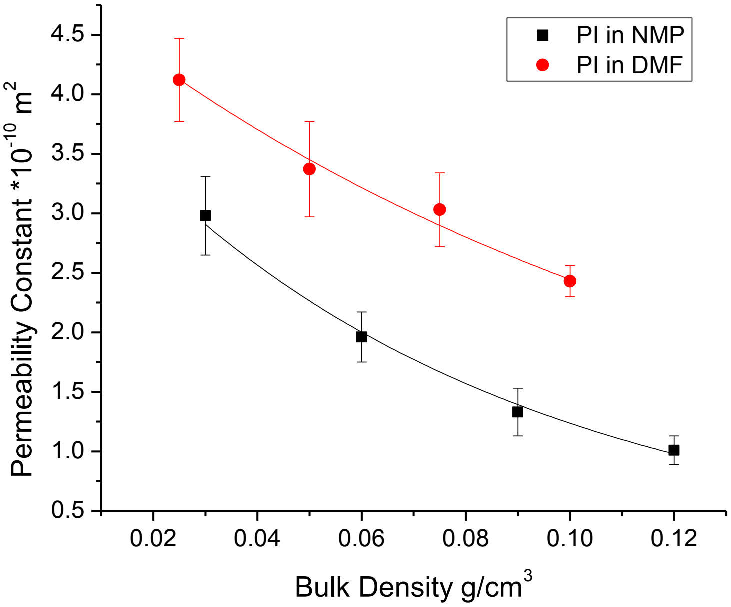

Figure 4.3 Permeability of PI aerogels vs. bulk density.

As seen in Figure 4.3, PI aerogels fabricated using DMF as the solvent show higher air permeability than the materials fabricated in NMP. This is attributed to higher values of porosity in the former. (Table 4.1) In addition, the total pore volume (shown in section 4.5) of DMF-based samples turned out to be larger than NMP-based aerogels. Note that skeletal densities of these two materials were almost the same. However, as we all know, aerogels are a unique class of materials inside which micropores, mesopores, and micropores coexist. It is not uniquely established yet as regards to what types of pores contribute the most to air permeability. Further investigation of surface area and pore size distribution may yield insight.

4.4 Filtration efficiency

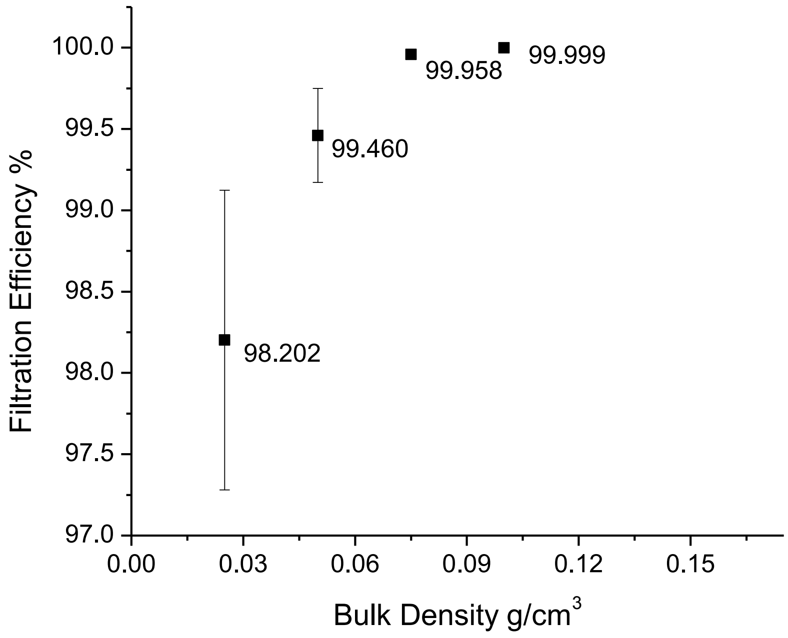

Figure 4.4 Filtration efficiency of DMF-based PI aerogels.

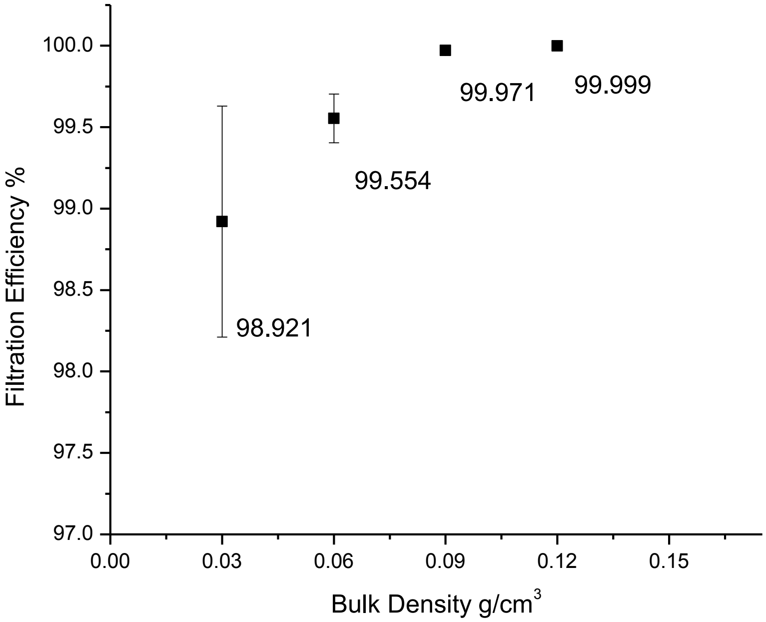

Figure 4.5 Filtration efficiency of NMP-based PI aerogels.

As shown in Figure 4.4 and 4.5, the values of filtration efficiency of both NMP-based and DMF-based specimens are greater than 99.95% for initial solids content in the gels at higher than 7.5 wt%. In view of this, the filter materials can be classified as high filtration efficiency filter media. The filtration efficiencies also show a power-law relationship with bulk density before reaching the maximum efficiency of the instrument, 99.999%, at bulk densities greater than 0.1 g/cm^3. Recall that the average size of generated sodium chloride nanoparticles in TSI-8130 tester was 75 nm. The particles of this size are considered as extremely hazardous to human body.

The data in Figure 4.4 and 4.5 also show that filtration efficiency values at lower bulk densities, e.g., for 0.025 g/cm^3 have large scatter. The standard deviation reduced to small values for aerogel bulk densities of 0.05 g/cm^3 or higher. In addition, the filtration efficiency data are almost independent of the nature of the solvents NMP or DMF used in sample preparation, although air permeability showed appreciable dependence on the solvents used.

4.5 Surface property

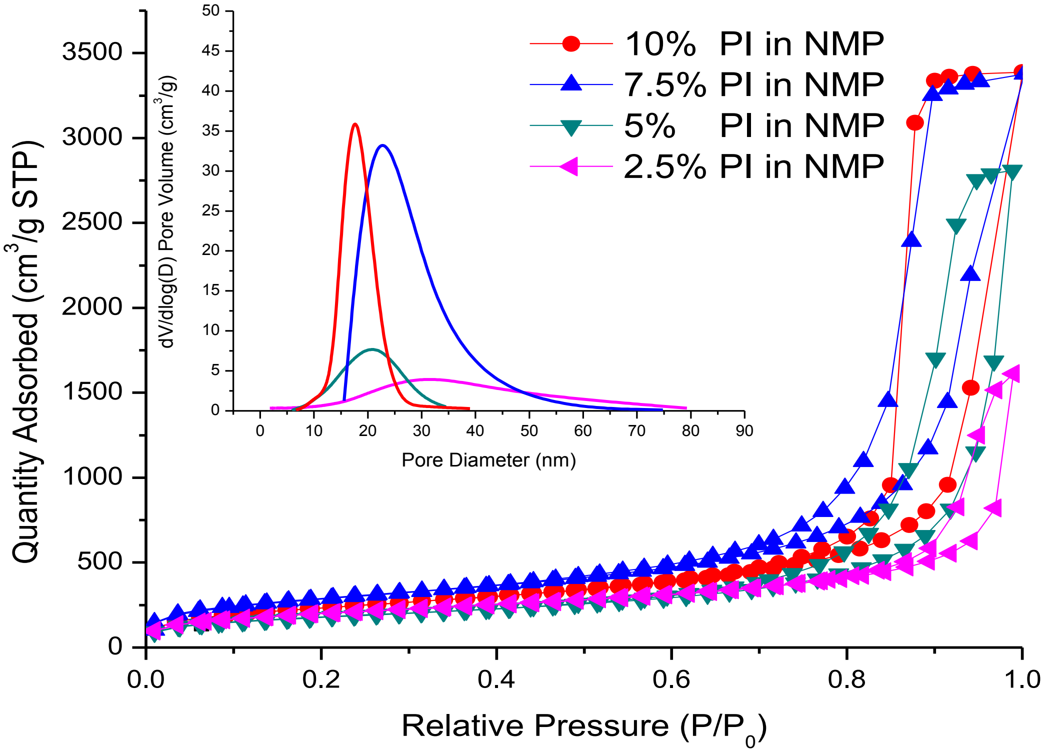

(a)

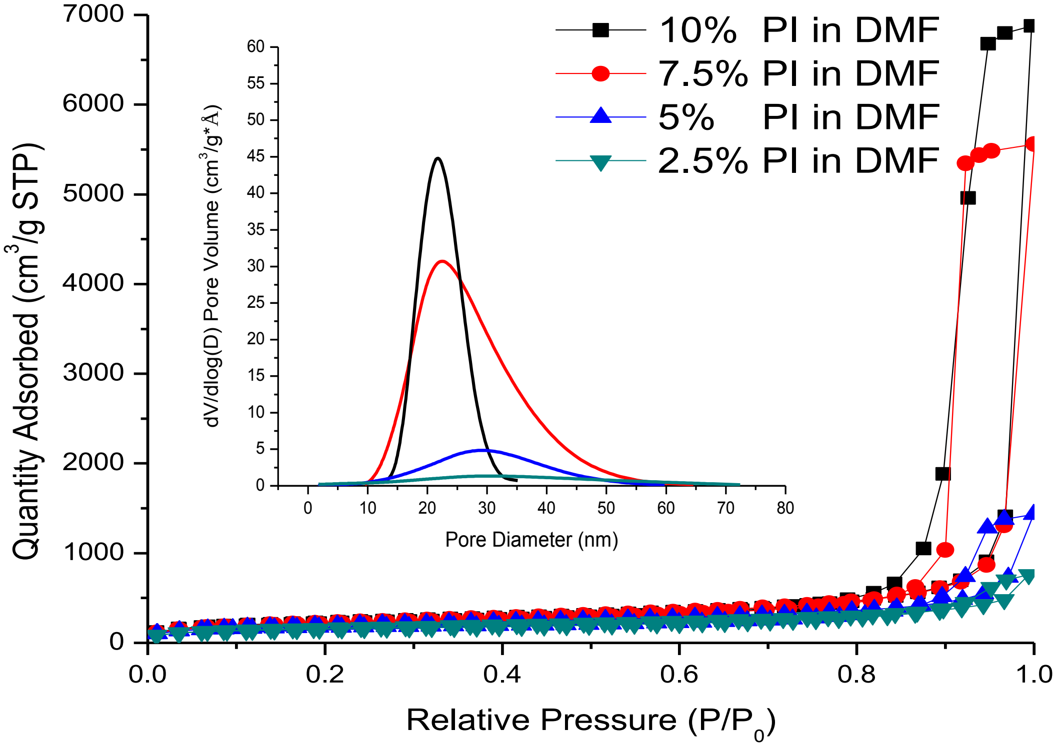

(b)

Figure 4.6 BET Isotherms and pore size distribution of (a) NMP-based PI and (b) DMF-based PI.

The BET isotherms and pore size distribution of PI aerogels are shown in Figure 4.6. The hysteresis loops are apparent in every BET isotherm curve. This indicates that mesopores existed in all specimens. The BET surface area values are presented in Figure 4.7. With an increase of the solids content, the surface area also increased from 473 m^2/g for 2.5% PI-NMP to 953 m^2/g for 10% PI-NMP. The NMP-based aerogels show higher surface area than DMF-based aerogels. The large pore volume of the mesopores in NMP (Table 4.2) contributes to higher surface area. As will be seen later, this is due to an increase of the solid network roughness. In NMP-based polyimide aerogels, the mesopore content (1.01 cm^3/g – 6.72 cm^3/g) is higher than in DMF-based aerogels (<1 cm^3/g). This establishes higher surface roughness of the building blocks of NMP-based PI than that in DMF-based PI.

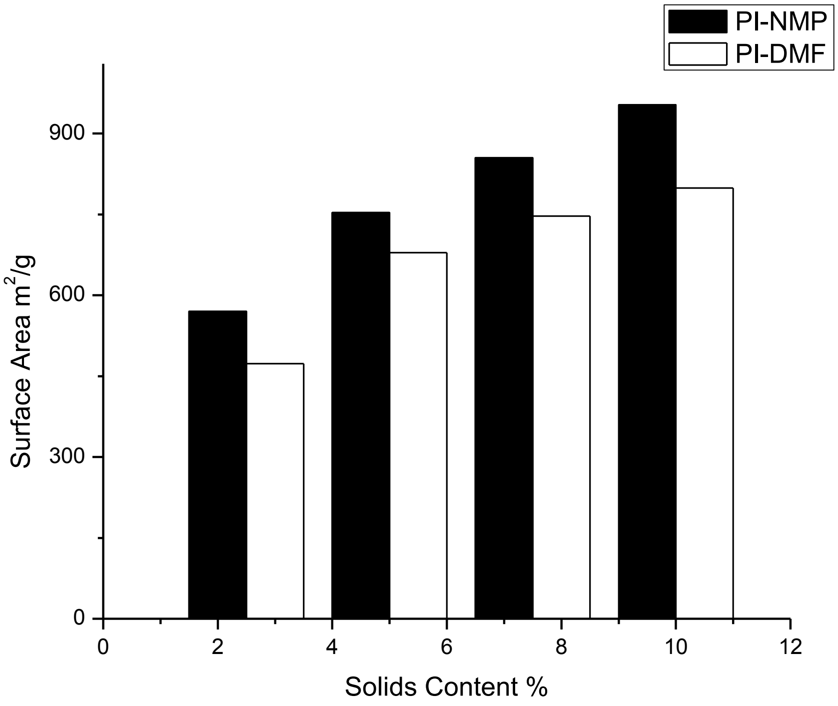

Figure 4.7 BET surface area of PI aerogel monoliths.

On the other hand, the fraction of macropores is higher in DMF-based specimens, as seen in Table 4.2. As a result, air permeability was higher. We believe that the fraction

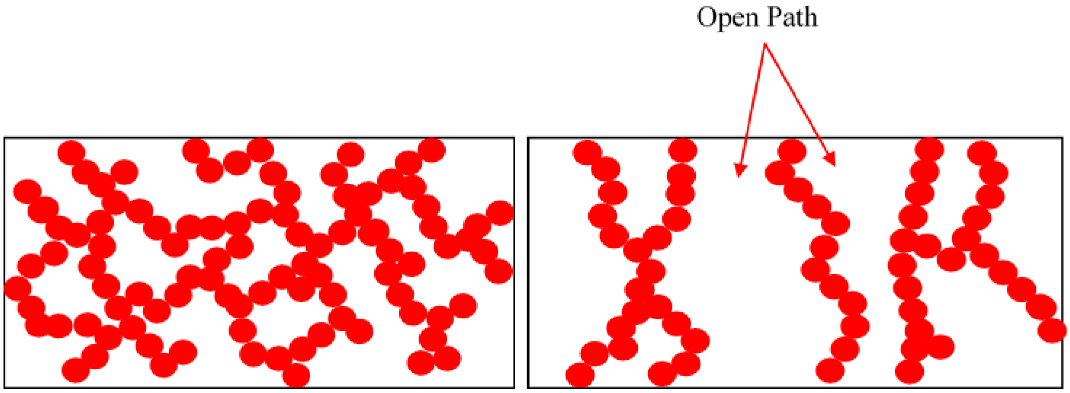

Figure 4.8 Schematic image of “open path” in PI aerogels.

of macropores exert the most important effect on air permeability of aerogel materials as only the macropores can provide “open path” for air flow (Figure 4.8). In the case of aerogel specimens with high solids content, the dense network structure can reduce the “open path” for air flow even though the porosity can be over 90%. For specimens with low solids content, more than 94% pores are macropores. This significantly increases the chance to create “open path” to air flow. As a result, air permeability is higher in this case.

Table 4.2 Total pore volume, pore volume of micropores, mesopores, macropores, and their fractions in PI aerogel monoliths.

Specimen	Total pore volume (cm^3/g)	Micropores pore volume (cm^3/g)	Mesopores Pore volume (cm^3/g)	Macropores pore volume (cm^3/g)	V'_{mi} (%)	$V'ms$ (%)	$V'ma$ (%)
2.5%PI-NMP	32.60	0.15	1.01	31.44	0.45	3.03	94.32
5.0%PI-NMP	16.51	0.08	1.92	14.51	0.46	11.14	84.19
7.5%PI-NMP	10.26	0.03	5.12	6.62	0.27	46.62	60.27
10%PI-NMP	7.56	0.03	6.72	0.81	0.36	81.27	9.80
2.5%PI-DMF	39.26	0.13	0.76	38.37	0.33	1.91	95.94
5.0%PI-DMF	18.88	0.15	0.81	17.92	0.77	4.13	91.41
7.5%PI-DMF	12.62	0.15	0.93	11.54	1.12	6.97	86.48
10%PI-DMF	9.20	0.12	1.34	8.74	1.21	13.53	88.28

To verify the above generalized anticipated outcome, the mentioned relationship between volume fraction of pores of different sizes and permeability was investigated. As seen in Figure 4.9 (a), a strong proportional effect of macropores on air permeability is observed for macropore volume fraction of 60% or higher. No obvious relationship, however, is captured for the micropores or mesopores. The plot of permeability vs. mesopore fractions (Figure 4.9 (c)) show data point which are complimentary to the data presented in Figure 4.9 (a). The data points in Figure 4.9 were obtained from PI aerogels prepared either in NMP or DMF.

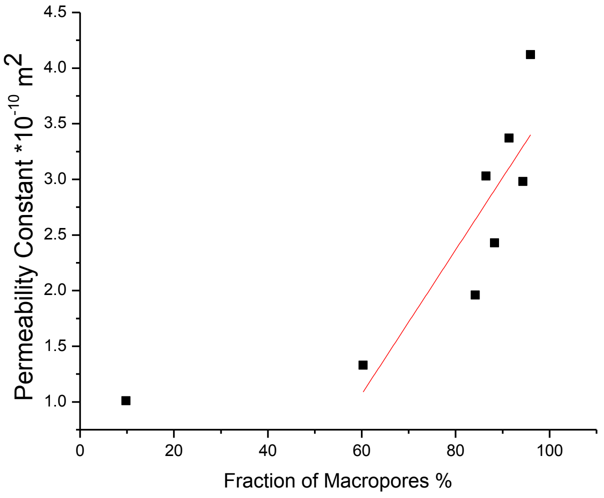

(a)

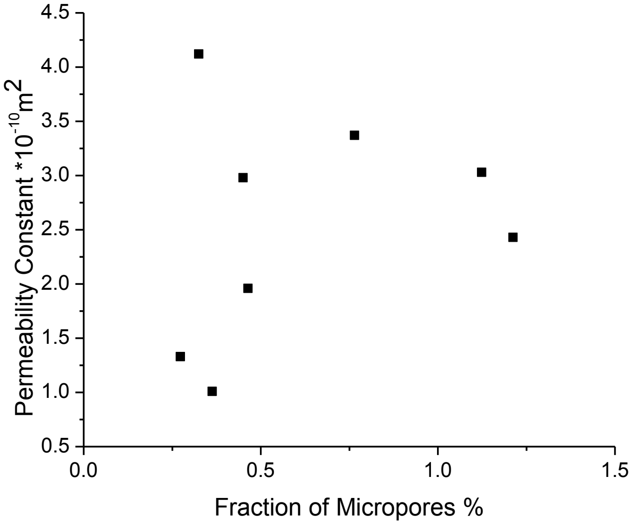

(b)

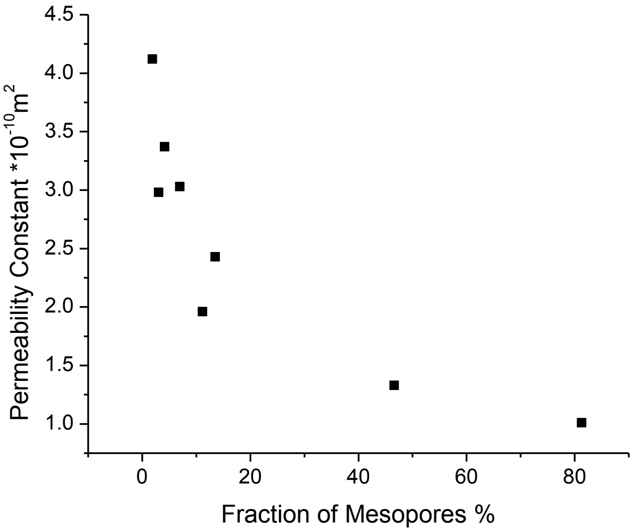

(c)

Figure 4.9 Effect of fraction of pores on air permeability of PI aerogels. (a) macropores, (b) micropores, and (c) mesopores.

4.6 Morphology

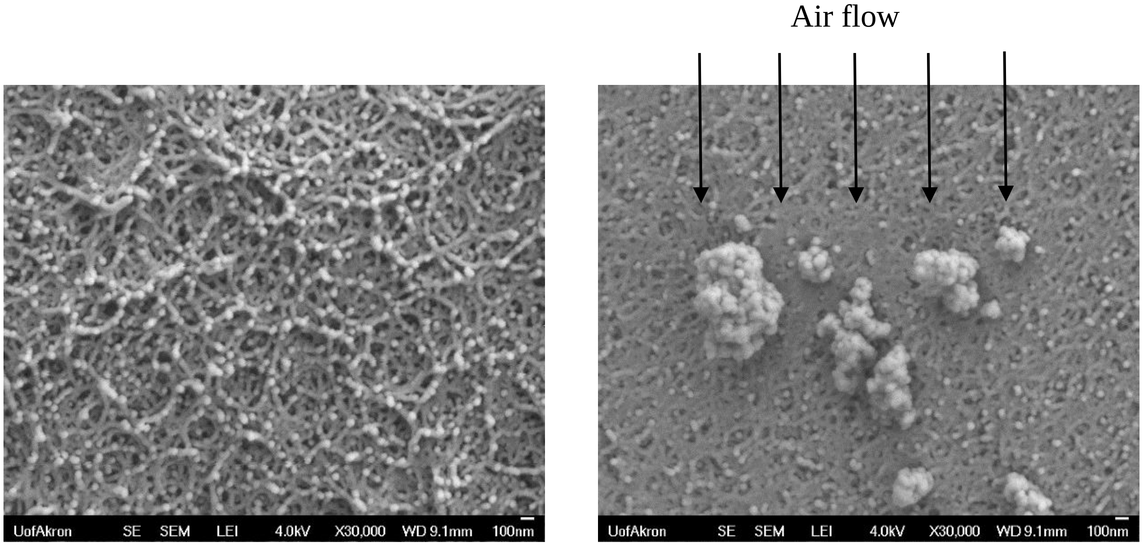

(a) (b)

Figure 4.10 SEM images of (a) inner network structure and (b) upper surface after filtration test of PI aerogels. Air flow direction is shown by the arrows.

Representative SEM images selected from 2.5% NMP-based polyimide aerogel specimen are shown in Figure 4.10. It is evident that the gel networks grew out of nucleation growth mechanism, Figure 4.10 (a). In Figure 4.10 (b), the sodium chloride particle aggregates of diameter around 50 nm are observed on the upper surfaces of the specimen. The image indicates that nanoparticles were successfully captured by the polyimide aerogel specimens. Furthermore, much denser network structure is observed on the upper surface of aerogel specimen than the inner body. This dense structure is called the “skin layer” which is ubiquitous in aerogel materials. The mechanism of formation of skin layer is still unclear but evaporation of the solvent and the fast gelation at the interfaces of the gels are considered important factors. The skin layer of PI aerogel played an important role in nanoparticle filtration, as evident in Figure 4.10 (b). The regime of high efficiency surface filtration was obtained.

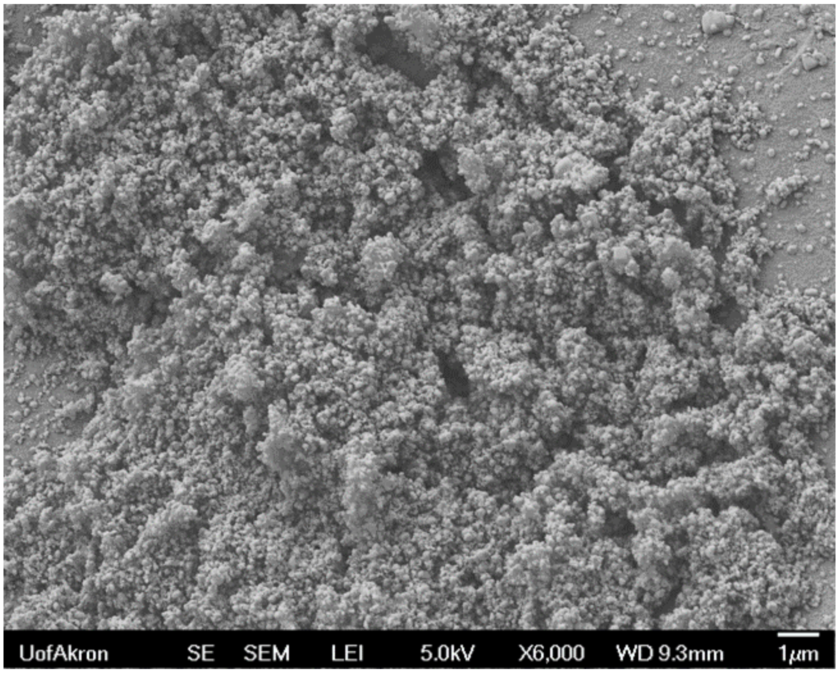

Figure 4.11 Upper surface of PI aerogel after passing the particle 100 times.

Figure 4.11 is taken from the upper surfaces of PI specimen after carrying out the filtration experiments for 100 times. The filtration efficiency of this sample grew from 98.20% to 99.999% during the multipass experiment. The open entrances at the surface of the specimens were almost filled by the nanoparticles. As a result, the air permeability reduced from 4.12×10^{-10} m^2 to 1.02×10^{-10} m^2.

4.7 Spectroscopic analysis

The chemical composition of PI aerogel was characterized by FTIR spectra as shown in Figure 4.12. The absorbance peaks at 1780 cm^{-1} and 1724 cm^{-1} refer to C=O symmetrical and asymmetrical stretching. The C-N linkage in imide rings is observed at absorbance peak of 1372 cm^{-1}. The peak at 724 cm^{-1} refers to C=O bending. Meanwhile, there is no strong peak observed at around 1550 cm^{-1} which belongs to C-NH. Thus, imidization of poly(amic acid) was completed, as was already inferred from the TGA data.

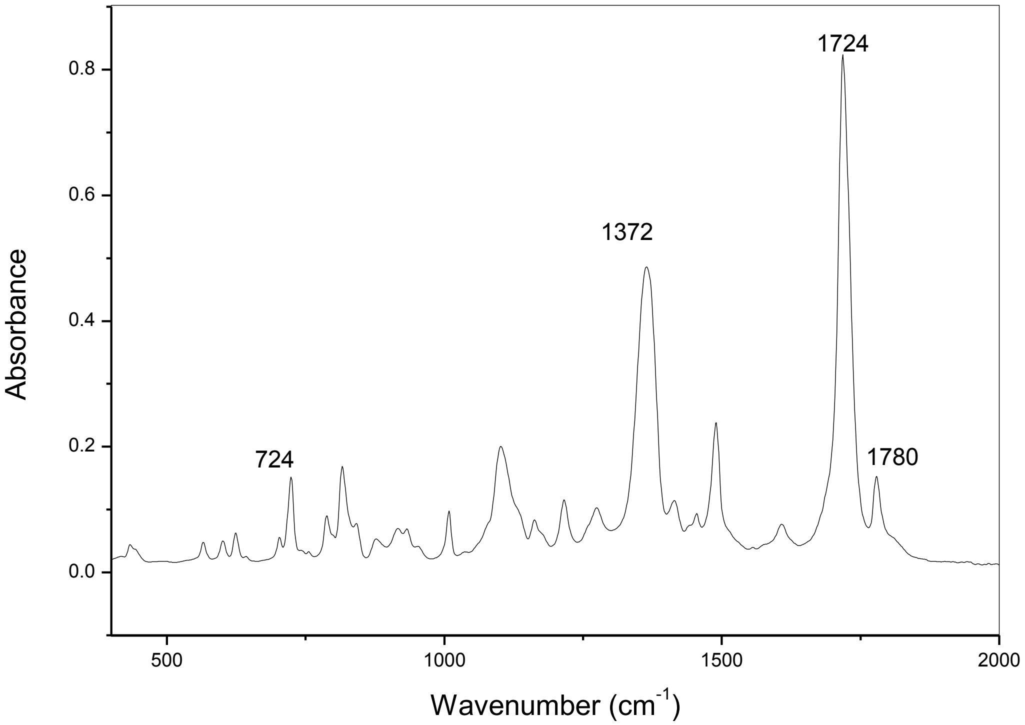

Figure 4.12 FTIR spectra of PI-DMF aerogel.

4.8 Conclusions

The potential of using polyimide aerogel monoliths for removal of airborne nanoparticles with mean diameter around 75 nm was verified. These materials derived from supercritical drying offered high porosity up to 98% due to large amount of macropores created inside. The large fraction of macropores (91%) can significantly increase air permeability (up to 4×10^{-10} m^2). Filtration efficiency of the specimens with high bulk densities (>0.075 g/cm^3) were found to be larger than 99.95% which is the classification limitation for high efficiency filters.

Due to outstanding thermal stability of polyimide aerogels, these monoliths show good potential for filtration of high temperature air flows. In this case, the cost of cooling down hot exhaust gas to manageable temperature can be eliminated if PI aerogels are used.

CHAPTER V

POLYIMIDE AEROGEL MICROPARTICLES PREPARED BY OIL-IN-OIL EMULSION SYSTEM

This chapter describes characterization of polyimide aerogel microparticles fabricated from oil-in-oil emulsion. In addition, the properties of aerogel microparticles are compared with those of monolithic PI aerogels.

5.1 Morphology

As shown in Figure 5.1 (a), PI aerogel microparticles do not have regular spherical shape. The shape deformation may have occurred during washing step in the Thinky Mixer. Note that solids content of polyimide sols used here was only 3% which quite possibly led to deformation of the gel particles. Mechanical properties of PI gels can be enhanced by adding extra solids but as a consequence, the sol would have high-viscosity, and gel too rapidly. This would prevent formation of a stable emulsion system. Figure 5.1 (b) shows the internal networks of PI aerogel microparticles. It is seen that there is no obvious difference of the internal structures of the gel particles with that of the monolithic PI specimens.

An interesting fibrous, stretched structure is obtained at the surfaces of the microparticles as seen in Figure 5.1 (c). Two possibilities are invoked here. First, the interfacial tension between the PI droplets in DMF and cyclohexane may have stretched the network. Second, during sol-gel reactions, the nucleation and growth may have started from the interface between the DMF-rich droplets and cyclohexane and as a result, compacted network at the surface was created. A schematic image of interfacial tension is shown in Figure 5.1 (d).

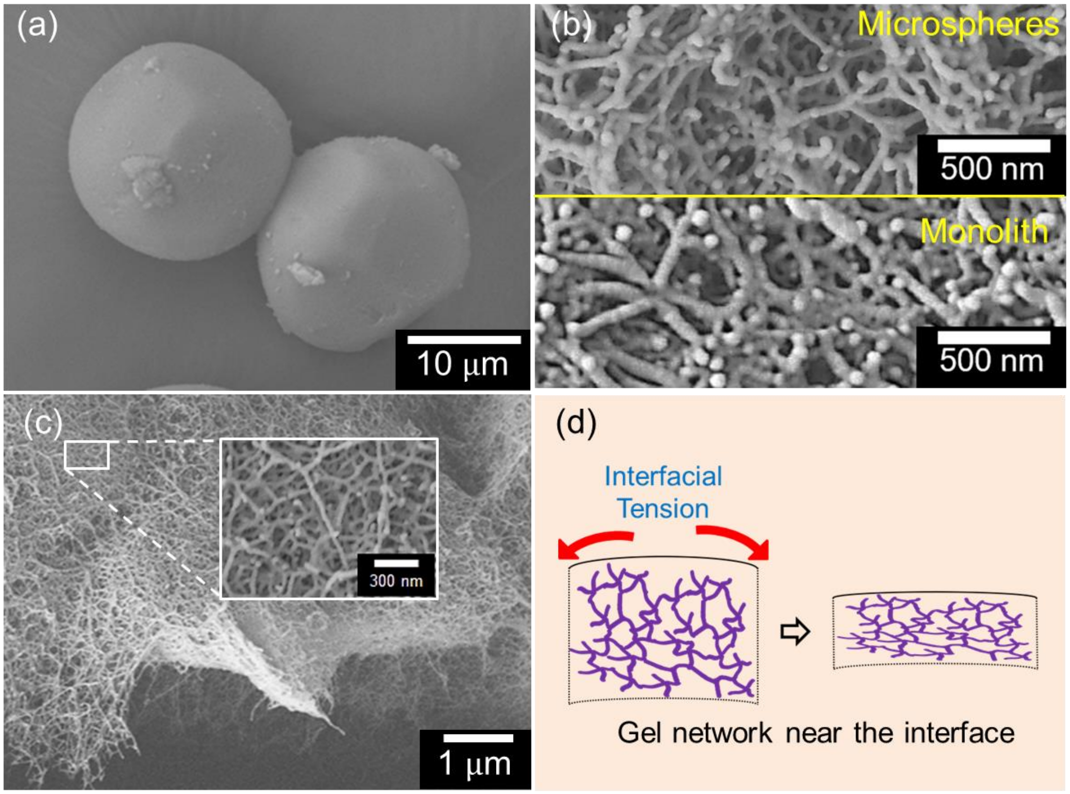

Figure 5.1 SEM images of (a) PI aerogel microparticles, (b) network of PI aerogel microparticles, (c) surface of PI aerogel miroparticles and (d) schematic image of effect of interfacial tension on gel network.

Table 5.1 lists the average diameter of PI aerogel microparticles and the diameter shrinkage values with the same solids content of 3% as with the monolith. Compared with

Table 5.1 Dimeter shrinkage of monolithic PI aerogel and microparticles.

	D_0	D	Diameter shrinkage (%)
Monolithic PI	32 mm	29.4 mm	8
PI aerogel Microparticles	41.8 µm	40.0 µm	4

the monolithic PI aerogels, the diameter shrinkage of microparticles is much smaller. This can be due to shortened diffusional length scale for solvent exchange.

5.2 Surface Property

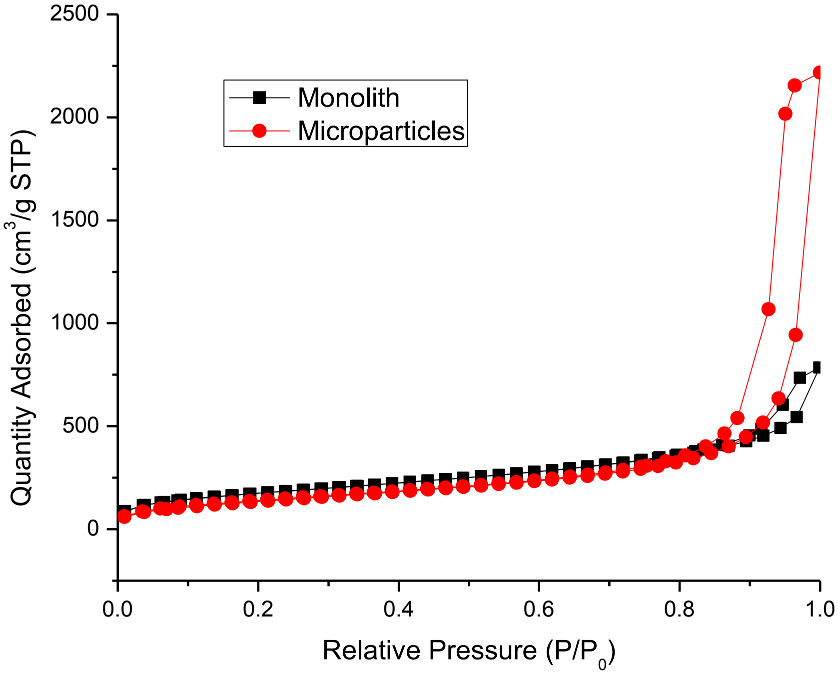

Figure 5.2 BET isotherms of PI aerogel monolith and microparticles.

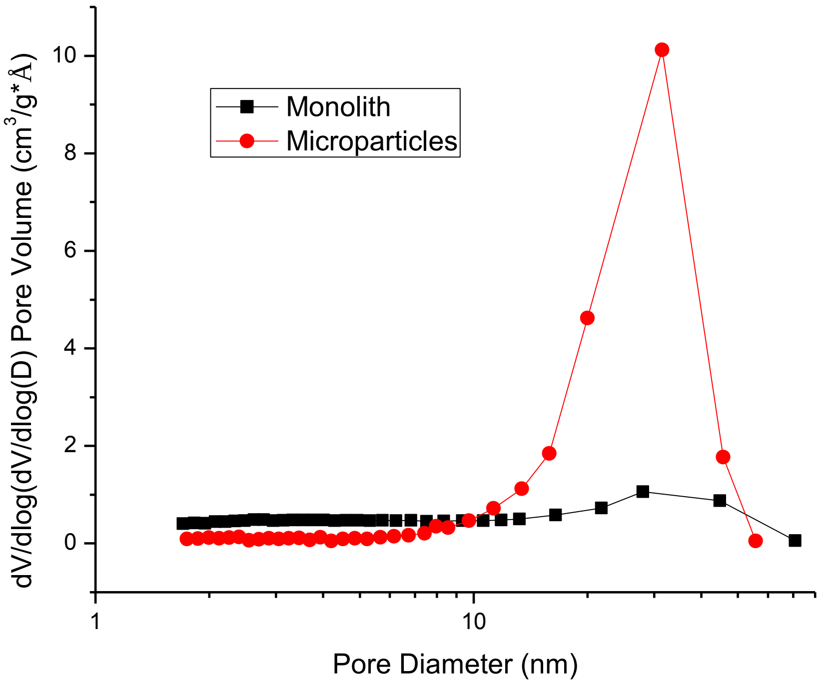

Figure 5.3 Pore size distribution of PI aerogel monolith and microparticles.

N_2-sorption isotherms and pore size distribution curves are presented in Figure 5.2 and Figure 5.3. In the case of monolith, the N_2-adsorption isotherm shows a sharp rise of adsorbed quantity at $P/P_0 > 0.9$, but a well-defined saturation plateau is not observed. This is an indication of the presence of both meso- and macropores with relatively lower mesopore content. In the case of aerogel microparticles, however, the N_2-desorption isotherm shows a short saturation plateau and a wider hysteresis loop, suggesting that the microspheres contained more mesopores than the monolithic sample. This conclusion is consistent with the pore size distribution curve in Figure 5.3. The area under the curve in Figure 5.3 approximately equals the cumulative pore volume. It is apparent that the aerogel microspheres had higher mesopore volume than the monolith. The data on pore volume and BET surface area of PI aerogels are summarized in Table 5.2. The PI microparticles contained higher pore volume than the monolith, e.g., 3.38 cm^3/g vs. 2.36 cm^3/g respectively and lower S_{BET}, e.g., 512 m^2/g vs. 716.7 m^2/g.

Table 5.2 BET surface area and specific pore volume of PI monoliths and microparticles

	BET surface area (m^2/g)	Pore volume between 1.7-300nm (cm^3/g)
Monolith	716.7	2.36
Microparticles	512.0	3.38

5.3 Spectroscopic Analysis

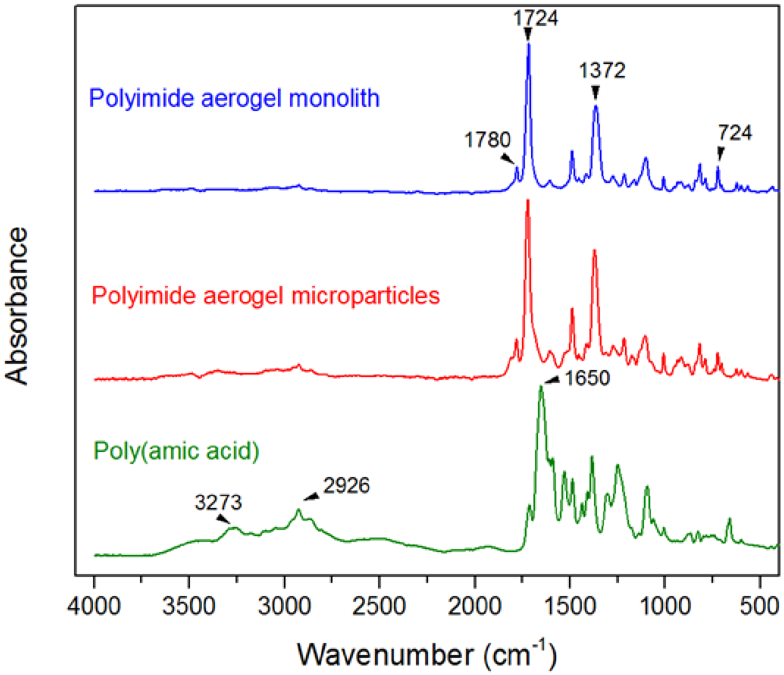

Figure 5.4 FTIR spectra of PI monolith, PI aerogel microparticles and poly(amic acid).

Figure 5.4 shows the IR spectra of crosslinked poly(amic acid), polyimide aerogel microparticles, and monolith. Strong absorbance at 1650 cm^{-1} indicates amide bonds in the poly(amic acid). In addition, the absorbance bands at around 2926 cm^{-1} and 3273 cm^{-1} correspond to the COOH and CONH groups in the poly(amic acid). After chemical imidization, the characteristic absorbance peaks of poly(amic acid) disappeared in the spectra of polyimide aerogel microparticles and monolith. The bands at around 1724 cm^{-1} and 1780 cm^{-1} are attributed to the symmetrical stretching and asymmetrical stretching of the imide C=O group respectively. The absorbance peak at 1372 cm^{-1} is associated with C-N stretching in the imide rings and the absorbance at 724 cm^{-1} is due to C=O bending. Besides, a visible but weak absorbance peak at around 2926 cm^{-1} for the microparticles indicates small quantities of unreacted COOH groups. Recall that polyimide gel microparticles were aged for shorter times than that of the corresponding monolith.

5.4 Conclusions

Aerogel microparticles of polyimide were produced via condensation polymerization in oil-in-oil emulsion. This is the first time that a method is reported using non-aqueous emulsion system to produce micrometer-sized aerogel particles. Compared with monolithic PI aerogels, PI aerogel microparticles showed lower surface area due to shorter aging time. However, the synthesis method used in this work reduced the diffusion length scale for solvent exchange and as a result, the degree of shrinkage of aerogel microparticles was effectively reduced.

CHAPTER VI

CONCLUSIONS

In this study, the potential of using monolithic polyimide aerogel (PI) as filter media for efficient removal of airborne nanoparticles was investigated. A new method of preparation of polyimide aerogel microparticles using oil-in-oil emulsion system was also introduced.

Aerogels are good materials for airborne nanoparticle filtration due to high porosity and 3-D network structures. Polyimide aerogels attract attention from the researchers due to this outstanding thermal stability and mechanical properties. At the same time, PI aerogels show high surface area as well as various sizes of pores. In this work, PI monolithic aerogels were synthesized from pyromellitic dianhydride (PMDA) and 2,2'-dimethylbenzidine (DMBZ). PI aerogels can be fabricated from various kinds of dianhydrides and diamines but here we selected PMDA and DMBZ due to their high solubility in solvents as well as high reactivity at room temperature. 1, 3, 5 triaminophenoxylbenzene (TAB) was selected as the crosslinking agent. N-methylpyrrolidinone (NMP) and dimethyl formamide (DMF) were used as solvents. NMP was the only solvent used at the beginning of this work. DMF was then used to identify a contrast in air permeability. The resultant PI specimens showed low bulk density (~0.025

to 0.12 g/cm^3) and large surface area (~400~800 m^2/g). High nanoparticle filtration efficiency (>99.95%) was obtained for these monoliths with relatively high bulk density (>0.05 g/cm^3). Note that depth filtration regime reported by Kim et al. [18] somewhat changed in this work to a combination of depth and surface filtration because of the skin layer. Most of nonaparticles were captured at the upper surface of PI aerogels where surface filtration occurred. The measurements showed that air permeability of these aerogels were in the order of 10^{-10} m^2. PI aerogels are known as mesoporous materials but here air permeability was as high as those of some macroporous aerogels like sPS aerogels. N_2 and CO_2 adsorption analysis were used for characterizing the pore structures of PI aerogels. The results showed that macropores contributed the most to total pore volume. Furthermore, the fraction of macropores had a siginificant effect on permeability of PI aerogels than the micropores or mesopores.

Aerogel microparticles of polyimide were produced via condensation polymerization in oil-in-oil emulsion. This emulsion was produced by dispersing in cyclohexane the droplets of PI sols in DMF solvent. Surfactants were used to stabilize the system. This is the first method that used non-aqueous emulsion system to produce micrometer-sized aerogel particles of PI. Compared with monolithic PI aerogels, PI aerogel microparticles showed lower surface area due to shorter aging time. However, the microparticles reduced the diffusion length scale for solvent exchange and as a result, the degree of shrinkage of aerogel microparticles.

REFERENCES

1. Raaschou-Nielsen, O.; Andersen, Z. J.; Beelen, R.; Samoli, E.; Stafoggia, M.; Weinmayr, G.; Hoffmann, B.; Fischer, P.; Nieuwenhuijsen, M. J.; Brunekreef, B.; Xun, W. W. Air pollution and lung cancer incidence in 17 European cohorts: prospective analyses from the European Study of Cohorts for Air Pollution Effects (ESCAPE). *Lancet oncol* **2013**, *14*, 813-822.

2. Marilena, K.; Castanas, E. Human health effects of air pollution. *Environ. Pollut.* **2008**, *151*, 362-367.

3. Mahowald, N. Aerosol indirect effect on biogeochemical cycles and climate. *Science* **2011**, 334, 794-796.

4. Querol, X.; Alastuey, A.; Ruiz, C.R.; Artiñano, B.; Hansson, H.C.; Harrison, R.M.; Buringh, E.T.; Ten Brink, H.M.; Lutz, M.; Bruckmann, P.; Straehl, P. Speciation and origin of PM10 and PM2. 5 in selected European cities. *Atmos. Environ.* **2004**, *38*, 6547-6555.

5. Zhang, R.; Jing, J.; Tao, J.; Hsu, S. C.; Wang, G.; Cao, J.; Lee, C. S. L.; Zhu, L.; Chen, Z.; Shen, Z. Chemical characterization and source apportionment of PM 2.5 in Beijing: seasonal perspective. *Atmos. Chem. Phys.* **2013**, *13*, 7053-7074.

6. Sunil, C.; Kenneth, L.; Cathy, L.; Mark, R.: Composite Porous Media Mott Metallurg Corp., 1999; Vol. WO9958223 (A1).

7. Duan, Y.; Jana, S. C.; Lama, B.; Espe, M. P.: Reinforcement of Silica Aerogels Using Silane-End-Capped Polyurethanes. *Langmuir* **2013**, *29*, 6156-6165.

8. Randall, J. P.; Meador, M. A. B.; Jana, S. C.: Tailoring Mechanical Properties of Aerogels for Aerospace Applications. *ACS Appl. Mater. Interfaces* **2011**, *3*, 613-626.

9. Pajonk, G. M. Transparent silica aerogels. *J. of Non-Cryst. Solids* **1998**, *225*, 307-314.

10. Wittwer V. Development of aerogel windows. *J Non-Cryst Solids* **1992**, 145, 233-236.

11. Ruben, G. C.; Pekala, R. W.: High-resolution transmission electron microscopy of the nanostructure of melamine-formaldehyde aerogels. *Journal of Non-Cryst. Solids* **1995**, *186*, 219-231.

12. Leventis, N.; Vassilaras, P.; Fabrizio, E. F.; Dass, A. Polymer nanoencapsulated rare earth aerogels: chemically complex but stoichiometrically similar core–shell superstructures with skeletal properties of pure compounds *J. Mater. Chem.* **2007**, *17*, 1502–1508.

13. Walendziewski, J.; Stolarski, M. Synthesis and properties of alumina aerogels. *React. Kinet. Catal. Lett.* **2000**, 71, 201–207.

14. Osaki, T.; Hoiuchi, T.; Sugiyama, T.; Suzuki, K.; Mori, T. Maintenance of large surface area of alumina heated at elevated temperatures above 1300° C by preparing silica-containing pseudoboehmite aerogel. *J. Non- Cryst. Solids* **1998**, 225, 111–114.

15. Wang, X.; Jana, S. C. Synergistic Hybrid Organic–Inorganic Aerogels. *ACS Appl. Mater. Interfaces* **2013**, *5*, 6423-6429.

16. Wang, X.; Jana, S. C. Syndiotactic polystyrene aerogels containing multi-walled carbon nanotubes. *Polymer* **2013**, *54*, 750-759.

17. Ahmed, M.S. and Attia, Y.A. Multi-metal oxide aerogel for capture of pollution gases from air. Appl. Therm. Eng. **1998**, *18*,787-797.

18. Kim, S. J.; Chase, G.; Jana, S.C. Polymer aerogels for efficient removal of airborne nanoparticles. *Sep. Purif. Technol.* **2015**, *156*, 803-808.

19. Kim, S.J.; Chase, G.; Jana, S.C. The role of mesopores in achieving high efficiency airborne nanoparticle filtration using aerogel monoliths. *Sep. Purif. Technol.* **2016** *166*, 48-54.

20. Farrar, P.A., Micron Technology, Inc. Foamed polymers, cured aerogels or air gaps as isulation medium; high density; integrated circuits. U.S. Patent **2004**, *6*,756,653.

21. Kawagishi, K.; Saito, H.; Furukawa, H.; Horie, K. Superior Nanoporous Polyimides via Supercritical CO_2 Drying of Jungle‐Gym‐Type Polyimide Gels. *Macromol. Rapid Commun.* **2007**, *28*, 96–100.

22. Meador, M.A.B.; Malow, E.J.; Silva, R.; Wright, S.; Quade, D.; Vivod, S.L.; Guo, H.; Guo, J.; Cakmak, M. Mechanically strong, flexible polyimide aerogels cross-linked with aromatic triamine. *ACS Appl. Mater. Interfaces* **2012**, *4*, 536-544.

23. Vivod, S.; Meador, M.A.B.; Cakmak, M.; Guo, H. Carbon nanofiber/polyimide aerogel thin film composites. *Polym. Prep.* **2011**, *52(2)*, 127-128.

24. Meador, M.A.B.; McMillon, E.; Sandberg, A.; Barrios, E.; Wilmoth, N.G.; Mueller, C.H.; Miranda, F.H. Dielectric and other properties of polyimide aerogels containing fluorinated blocks. *ACS Appl. Mater. Interfaces* **2014**, *6*, 6062-6068.

25. Meador, M.A.B.; Weber, A.S.; Hindi, A.; Naumenko, M.; McCorkle, L.; Quade, D.; Vivod, S.L.; Gould, G.L.; White, S.; Deshpande, K. Structure− Property Relationships in Porous 3D Nanostructures: Epoxy-Cross-Linked Silica Aerogels Produced Using Ethanol as the Solvent. *ACS appl. Mater. Interfaces* **2009**, 1, 894-906.

26. Simon, P.; Gogotsi, Y. Materials for Electrochemical Capacitors. *Nat. Mater.* **2008**, *7*, 845-854.

27. Lee, S. B.; Mitchell, D. T.; Trofin, L.; Nevanen, T. K.; Söderlund, H.; Martin, C. R. Antibody-based Bio-nanotube Membranes for Enantiomeric Drug Separations. *Science* **2002**, *296*, 2198-2200.

28. Sarawade, P. B.; Quang, D. V.; Hilonga, A.; Jeon, S. J.; Kim, H. T. Synthesis and Characterization of Micrometer-Sized Silica Aerogel Nanoporous Beads. *Mater. Lett.* **2012**, *81*, 37-40.

29. Cai, H.; Sharma, S.; Liu, W.; Mu, W.; Liu, W.; Zhang, X.; Deng, Y. Aerogel Microspheres from Natural Cellulose Nanofibrils and Their Application as Cell Culture Scaffold. *Biomacromolecules* **2014**, *15*, 2540-2547.

30. Kwon, J.; Kim, J.; Yoo, T.; Park, D.; Han, H. Preparation and Characterization of Spherical Polyimide Aerogel Microparticles. *Macromol. Mater. Eng.* **2014**, *299*, 1081-1088.

31. Pöschl, U. Atmospheric aerosols: composition, transformation, climate and health effects. *Angew. Chem. Int. Ed.* **2005**, *44*,7520-7540.

32. Milton, D. K.; Fabian, M. P.; Cowling, B.J.; Grantham, M. L.; McDevitt, J. J. Influenza virus aerosols in human exhaled breath: particle size, culturability, and effect of surgical masks. *PLoS Pathog* **2013**, 9, e1003205.

33. Heyder, J.; Gebhart, J.; Rudolf, G.; Schiller, C. F.; Stahlhofen, W.: Deposition of particles in the human respiratory tract in the size range 0.005–15 μm. *J. Aerosol Sci* **1986**, *17*, 811-825.

34. Zebida, O. A. Aerogel filters for removal of nanometric airborne particles LAP LAMBERT Academic Publishing **2011**

35. WHO: 7 million premature deaths annually linked to air pollution. *WHO: Geneva, Switzerland* **2014**, **2016**

36. www.3m.com Accessed on 04/21/2016

37. Li, Y.; Ma, T.; Kniss, D. A.; Lasky, L. C.; Yang, S.-T.: Effects of Filtration Seeding on Cell Density, Spatial Distribution, and Proliferation in Nonwoven Fibrous Matrices. *Biotechnol. Progr.* **2001**, *17*, 935-944.

38. Cushing, R. S.; Lawler, D. F.: Depth Filtration: Fundamental Investigation through Three-Dimensional Trajectory Analysis. *Environ. Sci. Technol.* **1998**, *32*, 3793-3801.

39. Brown, R. C. Air filtration: an integrated approach to the theory and applications of fibrous filters. *Pergamon Press*, **1993**

40. Stafford, R. G.; Ettinger, H. J.: Filter efficiency as a function of particle size and velocity. *Atmos. Environ.***1972**, *6*, 353-362.

41. http://www.asbestosguru-oberta.com/hepa.htm Accessed on 04/21/2016

42. Cushing, R.S.; Lawler, D.F. Depth filtration: Fundamental investigation through three-dimensional trajectory analysis. *Environ. Sci. Technol.* **1998**, *32*,3793-3801.

43. Brown, R. C.; Wake, D. Air filtration by interception—Theory and experiment. *J. Aerosol Sci.* **1991**, 22, 181-186.

44. Holdich, R. G.; Cumming, I. W.; Smith, I. D.: Crossflow microfiltration of oil in water dispersions using surface filtration with imposed fluid rotation. *J. Membrane Sci* **1998**, *143*, 263-274.

45. Kowalski, W. J.; Bahnfleth, W. P.; Whittam, T. S. Filtration of airborne microorganisms: modeling and prediction. *ASHRAE Transactions*, **1999**, *105*, 4.

46. Baetens, R.; Jelle, B. P.; Gustavsen, A. Aerogel insulation for building applications: a state-of-the-art review. *Energy and Buildings* **2011**, *43*, 761-769.

47. Armor, J. N.; Carlson, E. J.; Zambri, P. M. Aerogels as hydrogenation catalysts. *Appl. Catal.* **1985**, *19*, 339-348.

48. Kistler, S. S. Coherent Expanded Aerogels and Jellies. *Nature* **1931**, *127*, 741.

49. Duan, Y.; Jana, S.C.; Lama, B.; Espe, M. P. Reinforcement of silica aerogels using silane-end-capped polyurethanes. *Langmuir* **2013**, *29*, 6156-6165.

50. Beltrán-Osuna, A. A.; Cao, B.; Cheng, G.; Jana, S. C.; Espe, M. P. and Lama, B. New antifouling silica hydrogel. *Langmuir* **2012**, *28*, 9700-9706.

51. Schaefer, D. W.; Keefer, K. D. Structure of random porous materials: silica aerogel. *Phys. Rev. lett.* **1986**, *56*, 2199.

52. Morris, C. A.; Anderson, M. L.; Stroud, R. M.; Merzbacher, C. I.; Rolison, D. R. Silica sol as a nanoglue: flexible synthesis of composite aerogels. *Science* **1999**, *284*, 622-624.

53. Tsutsui, T.; Yahiro, M.; Yokogawa, H.; Kawano, K.; Yokoyama, M. Doubling Coupling‐Out Efficiency in Organic Light‐Emitting Devices Using a Thin Silica Aerogel Layer. *Adv. Mater.* **2001**, *13*, 1149-1152.

54. Shinko, A.; Jana, S. C.; Meador, M. A. Crosslinked polyurea aerogels with controlled porosity. *RSC Advances* **2015**, *5*, 105329-105338.

55. Meador, M. A. B.; Alemán, C. R.; Hanson, K.; Ramirez, N.; Vivod, S.L.; Wilmoth, N.; McCorkle, L. Polyimide Aerogels with Amide Cross-Links: A Low Cost Alternative for Mechanically Strong Polymer Aerogels. *ACS Appl. Mater. Interfaces* **2015**, *7*, 1240-1249.

56. Pekala, R.W. Organic aerogels from the polycondensation of resorcinol with formaldehyde. *J. Mater. Sci.* **1989**, *24*, 3221-3227.

57. Dorcheh, A. S.; Abbasi, M. H. Silica aerogel: synthesis, properties and characterization. *J. Mater. Process. Technol.* **2008**, *199*, 10-26.

58. Kim, G. S.; Hyun, S. H.; Park, H. H. Synthesis of Low‐Dielectric Silica Aerogel Films by Ambient Drying. *J. Am. Ceram. Soc.* **2001**, 84, 453-55.

59. Mizushima.; Yasuyuki.; Hori, M. Alumina aerogel for support of a methane combustion catalyst. *Appl.Catal. A* **1992**, *88*, 137-148.

60. Pekala, R. W. Organic aerogels from the polycondensation of resorcinol with formaldehyde. *J. Mater. Sci.* **1989**, *24*, 3221-3227.

61. Gu, S.; Li, Z.; Miyoshi, T.; Jana, S. C. Polybenzoxazine aerogels with controllable pore structures. *RSC Advances*, **2015**, *5*, 26801-26805.

62. Biesmans, G.; Mertens, A.; Duffours, L.; Woignier, T.; Phalippou, J. Polyurethane based organic aerogels and their transformation into carbon aerogels. *J. Non-cryst. Solids* **1998**, *225*, 64-68.

63. Shinko, A. Structure and morphology control in polymer aerogels with low crosslink density. PhD. Dissertation, The University of Akron, **2015**

64. Wang, X. Tailoring of pore structures and surface properties of syndiotactic polystyrene aerogels. PhD. Dissertation, The University of Akron, **2013**

65. Mulik, S.; Sotiriou-Leventis, C. Resorcinol-formaldehyde aerogels. *Aerogels Handbook* **2011**, 215-234.

66. Cooper, D. W. Theoretical study of a new material for filters: aerogels. *Part. Sci. Technol.* **1989**, 7, 371-380.

67. Kong, F. M.; LeMay, J. D.; Hulsey, S. S.; Alviso, C. T.; Pekala, R. W. Gas permeability of carbon aerogels. *J. Mater. Res.* **1993**, *8*, 3100-3105.

68. Cao, S.; Yeung, K. L.; Kwan, J. K. C.; To, P. M. T.; Yu, S. C. T.: An investigation of the performance of catalytic aerogel filters. *Appl. Catal. B* **2009**, *86*, 127-136.

69. Meador, M. A. B.; Malow, E. J.; He, Z. J.; McCorkle, L.; Guo, H.; Nguyen, B.N. Synthesis and properties of nanoporous polyimide aerogels having a covalently bonded network structure. *Polym. Prepr.* **2010**, *51*, 265–266.

70. Guo, H.; Meador, M. A. B.; McCorkle, L.; Quade, D. J.; Guo, J.; Hamilton, B.; Cakmak, M.; Sprowl, G. Polyimide aerogels cross-linked through amine functionalized polyoligomeric silsesquioxane. *ACS Appl. Mater. Interfaces* **2011**, *3*, 546-552.

71. Nguyen, B.N.; Meador, M.A.B.; Ercegorvic, S.; Rohovie, M.; McCorkle, L.; Guo, J.; Li, L.; Hamilton, B.H.; Quade, D.J. Development of high temperature, flexible polyimide aerogels. *Polym. Prepr.* **2011**, *52*, 256.

72. Chidambareswarapattar, C.; Larimore, Z.; Sotiriou-Leventis, C.; Leventis, N. Porous nanostructured polyimide etworks and methods of manufacture. *Polym. Prep.* **2010**, *51*, 638-639.

73. Chidambareswarapattar, C., Sotiriou-Leventis, C. and Leventis, N. One-step polyimide aerogels from anhydrides and isocyanates. **2010**

74. Vivod, S.; Meador, M.A.B.; Cakmak, M.; Guo, H. Carbon nanofiber/polyimide aerogel thin film composites. *Polym. Prep.* **2011**, *52*, 127-128.

75. Nguyen, B.N.; Meador, M.A.B.; Rowan, S.; Cudjoe, E.; Sandberg, A. Polyimide Cellulose Nanocrystal Composite Aerogels. **2014.**

76. Koerner, H.; Strong, R. J.; Smith, M. L.; Wang, D. H.; Tan, L. S.; Lee, K. M.; White, T. J.; Vaia, R. A. Polymer design for high temperature shape memory: Low crosslink density polyimides. *Polymer* **2013**, *54*, 391-402.

77. Brinker, C. J. Sol-gel Science: The Physics and Chemistry of Sol-Gel Processing. Academic Press, INC **1990**

78. Pajonk, G. M. Drying methods preserving the textural properties of gels. *J. Phys. Colloq.* **1989**, *50*, 13–22.

79. Egeber E. D.; Engel, J. Freeze-drying of silica gels prepared from siliciumethoxide. *J. Phys. Colloq.***1989**, *50*, 23–28

80. Einarsrud M-A, Kirkedelen MB, Nilsen E, Mortensen K, Samseth J Structural development of silica gels aged in TEOS. *J. Non-Cryst. Solids* **1998**, *231*, 10–16

81. Chen, J. H.; Ruckenstein, E. Surface Modification by a 2-Phase Deposition of a Surfactant. *J. Colloid Interf. Sci.* **1991**, *142*, 544-553.

82. Chan, J. B.; Jonas, J. Effect of Various Amide Additives on the Tetramethoxysilane Sol-Gel Process. *J. Non-Cryst. Solids* **1990**, 126, 79-86.

83. Alié, C.; Tcherkassova, N.; Ferauche, F.; Lambert, S.; Heinrichs, B.; Pirard, R.; Pirard, J. P. Multigram scale synthesis and characterization of low-density silica xerogels. *J. Non-Cryst. Solids* **2006**, *352*, 2763-2771.

84. Brunauer, S.; Emmett, P.H.; Teller, E. Adsorption of gases in multimolecular layers. *J. Am. Chem. Soc.* **1938**, *60*, 309-319.

85. Raghavan, B. Nanofiber Filter Media for Air Filtration: Experimental and Modeling Study, Ph.D. Thesis, University of Akron, Akron, OH, USA, **2010**, 85.

86. Patel, S. U.; Manzo, G. M.; Patel, S. U.; Kulkarni, P. S.; Chase, G. G. Permeability of electrospun superhydrophobic nanofiber mats. *J. Nanotechnol.* **2012**, *2012*, 483976.